Phtodetection Characteristics of Metamorphic HEMT and its Application for Radio-on-fiber systems

Hyo-Soon Kang

The Graduate School

Yonsei University

Department of Electrical and Electronic Engineering

Phtodetection Characteristics of Metamorphic HEMT and its Application for Radio-on-fiber systems

A Master's Thesis

Submitted to the Department of Electrical and Electronic Engineering

and the Graduate School of Yonsei University

in partial fulfillment of the

requirements for the degree of

Master of Science

Hyo-Soon Kang

January 2004

This certifies that the master's thesis of Hyo-Soon Kang is approved.

_____

Thesis Supervisor: Woo-Young Choi

_____

Ilgu Yun

_____

Sangin Kim

The Graduate School

Yonsei University

January 2004

Contents

Figure Index

Abstract

Photodetction Characteristics of Metamorphic HEMT and its Application for Radio-on-fiber systems

By

Hyo-Soon Kang

Department of Electrical and Electronic Engineering

The Graduate School

Yonsei University

In this thesis, photodetection characteristics of metamorphic high-electron-mobility transistor (HEMT) on GaAs substrate and its applications for radio-on-fiber are demonstrated. Fist of all, the epitaxial layer structure and electrical behavior of the metamorphic HEMT are examined in order to characterize the intrinsic device properties.

To investigate the photodetection characteristics of the device, photodetection mechanisms are clarified under different operating conditions with DC and modulated optical signal. Through the

experiments, it is verified that the photovoltaic effect is dominant under turn-on condition and the photoconductive effect under turn-off condition. In addition, optical modulation responses and photodetection process dependent on the bias voltage are examined in the metamorphic HEMT.

For the application of radio-on-fiber systems, optoelectronic mixers and direct optical injection-locked oscillators are implemented. Using the optoelectronic mixer based on the metamorphic HEMT, frequency up-conversion is performed in wide LO frequency range and SFDR as well as their internal conversion efficiency is measured. In the experiment of direct optical injection-locked oscillator, 10 GHz phase locked oscillator is realized with the injection of modulated optical signal. The locking range and phase noise characteristics are investigated.

From theses results, it is expected that the metamorphic HEMT can be utilized for antenna base station architecture in radio-on-fiber systems.

Keywords: metamorphic HEMT, radio-on-fiber system, photodetection, phototransistor, photovoltaic effect, photoconductive effect, SFDR, optoelectronic mixer, optical injection-locked oscillator

Ⅰ. Introduction

Recently, there has been an increasing interest in the use of fiber-optic technique in broadband wireless communication systems because of the advantages of optical fiber including low loss, wide bandwidth capability, compact size and flexibility [1]. This merging of wireless and optical communication system is so called radio-on-fiber (RoF) system. Since a number of antenna base stations are required in millimeter-wave radio-on-fiber system due to large radiation loss, it is important to realize single chip integration and low cost of antenna base station.

There are two schemes for implementing the radio-on-fiber systems. One configuration is that optically generated millimeter-wave signal is distributed via optical fiber and then converted back to millimeter-wave at the antenna base station. However, this scheme has some problems, which are difficulties of optical millimeter-wave generation [2] and chromatic dispersion characteristics of optical fiber [3]. In addition, high speed photodetectors are required to convert optical signal to millimeter-wave signal.

The other configuration is remote up-conversion scheme. The intermediate frequency (IF) signal embedded in optical carrier is

transmitted through optical fiber after that photodetection and frequency up-conversion to millimeter-wave band is performed at the base station. Fig. 1.1 shows the block diagram of remote up-conversion scheme in radio-on-fiber system. However, in this configuration, many microwave components such as microwave mixers, local oscillators and amplifiers as well as photodetectors are required. Furthermore, it has a difficulty of monolithic integration between optical and microwave components due to different device structures.

Indium phosphide (InP) based high electron mobility transistors (HEMTs) have been a strong candidate for simplifying the antenna base station architecture. InP HEMTs are widely used in microwave components such as RF amplifier, mixer and oscillator due to intrinsic high speed characteristics. Besides, they can provide not only photodetection to 1.55 ㎛ optical signal but also new functionalities including optoelectronic mixing [4] and optical injection-locked oscillation [5]. Utilizing the InP HEMT as a photodetector or optoelectronic components, a single chip integration can be possible between optical and microwave components using monolithic microwave integrate circuit (MMIC) process. Although there are benefits of InP HEMTs, they have inherent disadvantages, which are low breakdown voltage characteristics, high cost and fragile InP

substrate.

To overcome these problems, gallium arsenide (GaAs) based metamorphic HEMT has been regarded as an alternative to InP-based HEMT because it provides high breakdown voltages and compatibility to mature GaAs-based MMIC process [6]. Using the InAlAs graded buffer layer, the metamorphic HEMT has shown high speed performance as well as high power capability

In this thesis, photodetection characteristics of the metamorphic HEMT on GaAs substrate and its applications for radio-on-fiber system are demonstrated. In chapter 2, device structures and fundamentals of InP HEMTs and metamorphic HEMTs are explained. The description of metamorphic HEMT used in this thesis is also included. In chapter 3, the electrical characteristics including DC and microwave properties of the device used in this thesis are described. In chapter 4, photodetection characteristics of the metamorphic HEMT under illumination of DC and modulated optical signal are experimentally examined. The photodetection mechanisms, the photovoltaic and photoconductive effect, are also clarified. In chapter 5, optoelectronic mixers and direct injection-locked oscillators based on metamorphic HEMTs for the application of radio-on-fiber system are implemented and their performances are evaluated.

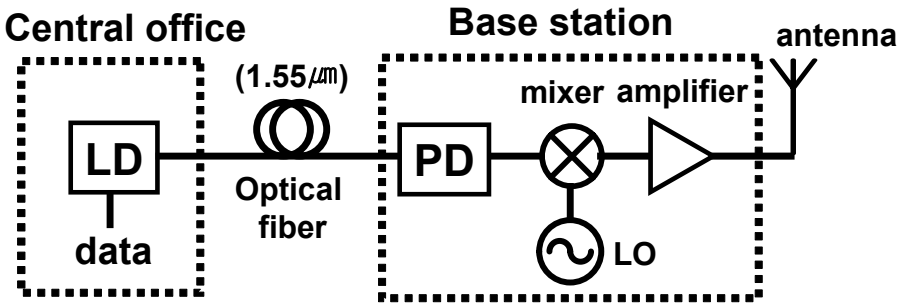

Figure 1.1 Block diagram of remote up-conversion scheme in radio-on-fiber system.

Ⅱ. Background

The High-Electron-Mobility Transistor (HEMT) is a heterostructure filed-effect transistor. To enhance electron mobility, intrinsic channel layer, which is immune to impurity scattering, is realized using different band gap materials [7, 8]. Other names also used for the device are Two-dimensional Electron Gas Field-Effect Transistor (TEGFET), Heterostructure Filed-Effect Transistor (HFET), Selectively Doped Heterostructure Transistor (SDHT) and Modulation-doped FET (MODFET). The name of HEMT is used in this thesis.

A. InP-based high-electron-mobility transistor

Fig. 2.1 shows a typical epitaxial layer structure and the energy band diagram for a conventional lattice-matched InAlAs/InGaAs/InP HEMT [8]. The InP HEMT is fabricated with the heterostructure epitaxial layers grown on a semi-insulating InP substrate by using molecular beam epitaxy (MBE) or metal-organic chemical vapor deposition (MOCVD). The epitaxial layer is composed of $In_{0.52}Al_{0.48}As$ barrier layer, $In_{0.52}Al_{0.48}$ spacer layer, $In_{0.53}Ga_{0.47}As$ channel layer and $In_{0.52}Al_{0.48}As$ buffer layer, from top to bottom. Between the barrier and

spacer layer, doping is applied for supplying electrons to the channel layer. The source and drain contacts are ohmic while the gate is a Schottky barrier. The important feature of the device is intrinsic InGaAs channel layer. By adopting the heterojunction between wide band gap material ($In_{0.52}Al_{0.48}As$) and narrow band gap material ($In_{0.53}Ga_{0.47}As$), the potential well is formed by conduction band discontinuity. Thus, the electrons are confined in the potential well. These localized electrons in the channel are described as a two-dimensional electron gas (2DEG) as shown in Fig. 2.1 (b). Electrons traveling in this region do not suffer impurity scattering because the $In_{0.53}Ga_{0.47}As$ channel layer is undoped. As a result, high electron mobility is realized, whose value is about 11,000 cm^2/Vs at room temperature.

The operation mechanism of the InP HEMT is similar to the metal-semiconductor filed-effect transistor (MESFET) [9]. The drain-source bias causes the longitudinal electric filed in the channel and gate bias control the carrier concentration of the 2DEG. With decreasing the gate voltage, the electron concentration in 2DEG decreases. Below the threshold voltage of the gate bias, the sheet carrier concentration of 2DEG becomes negligibly small and the channel is pinched off.

Due to the structural advantages of InP HEMT, there have been

many works for enhancing the operation frequency of the device. Since 1990s, several works have shown that InP-based HEMTs can exhibit a high cutoff frequency, f_T, in the sub-millimeter-wave frequency range (300 GHz to 3 THz) when the gate length is reduced. In addition, to increase the electron mobility of the channel, pseudomorphic HEMT has been proposed. By changing the InAl mole fraction of cannel layer ($In_xGa_{1-x}As$), the high speed performance was achieved due to enhanced electron mobility with strained layer caused by lattice mismatch of InAlAs/InGaAs layers [8]. Until now, the ultrahigh f_T of 562 GHz for a 25-nm-long-gate pseudomorphic InAlAs/InGaAs HEMT is reported [10].

As mentioned early, the InP HEMT is suitable for fiber-optic applications because it can detect 1.55 ㎛ optical signal. Since the band gap energy of $In_{0.53}Ga_{0.47}As$ (0.74 eV) channel layer is lower than the incident photon energy (0.8 eV), optical signals can be absorbed in the channel layer and generate electron-hole pairs.

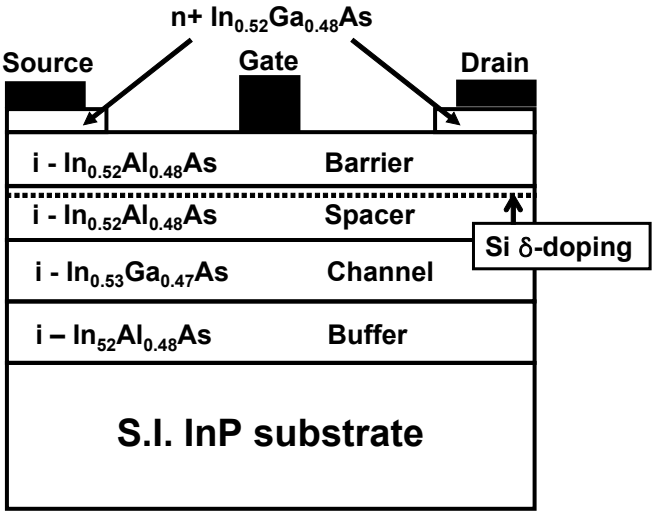

(a)

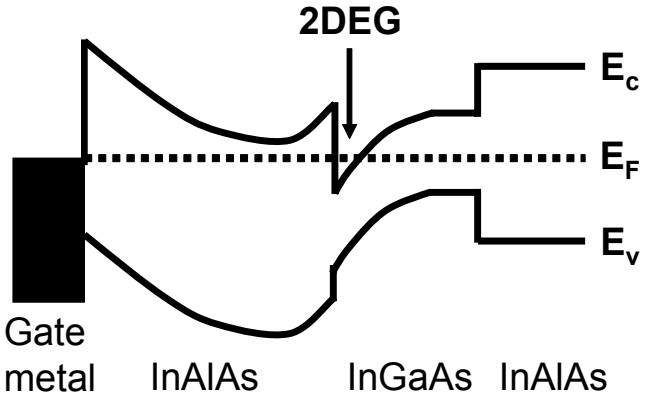

(b)

Figure 2.1 Conventional lattice-matched InP HEMT (a) Epitaxial layer structure (b) Energy band diagram. E_c is conduction band, E_v is valence band and E_F is fermi level.

B. Metamorphic high-electron-mobility transistor used in this thesis

Because InP substrates are more expensive than GaAs substrates, it is desirable to combine the advantages of heterostructure with the low cost and availability of large size GaAs wafers. In this reason, metamorphic HEMT is developed. Using a metamorphic buffer layer, InP-based high electron mobility transistors can be grown on GaAs substrates [11, 12]. By utilizing a sufficiently thick buffer layer, the metamorphic HEMTs have not only high carrier transport property as in the InP HEMT but also compatibility to the GaAs substrate. Fig. 2.2 shows the epitaxial layer structure of the metamorphic HEMT used in this thesis[1]. The epitaxial layers are made up of graded $In_xAl_{1-x}As$ buffers which are used to mitigate problems associated with lattice mismatch, composite channels with 20 nm $In_{0.35}Ga_{0.65}As$ and 10 nm $In_{0.53}Ga_{0.47}As$ layers, 4.5 nm $In_{0.35}Al_{0.65}As$ spacer with Si delta-doping ($5\times10^{12}\,cm^2$), 15 nm $In_{0.35}Al_{0.65}As$ barrier, and 10 nm n^+ $In_{0.35}Ga_{0.65}As$ capping layer, from bottom to top.

In a conventional InAlAs/InGaAs material system, the device suffer from the low breakdown voltage characteristics due to the enhanced

[1] The metamorphic HEMT used in this thesis is fabricated by Dae-Hyun Kim and Kwang-Seok Seo at the inter-university semiconductor research center (ISRC) in Seoul National University.

impact ionization in the narrow band gap of $In_{0.53}Ga_{0.47}As$ channel, which causes the reduction of on-state and off-state breakdown voltage. To avoid this problem, $In_{0.53}Ga_{0.47}As/In_{0.35}Ga_{0.65}As$ composite channels are used for improving carrier transport characteristics without sacrificing breakdown voltages for high power performance.

Hall measurements at room temperature showed that electron mobility and two-dimensional electron gas (2DEG) density are 9370 $cm^2/V{\cdot}s$ and 2.3×10^{12} $/cm^2$, respectively. The metamorphic HEMT used in this thesis has T-shaped gate, whose length and width are 0.25 ㎛ and 50 ㎛, respectively.

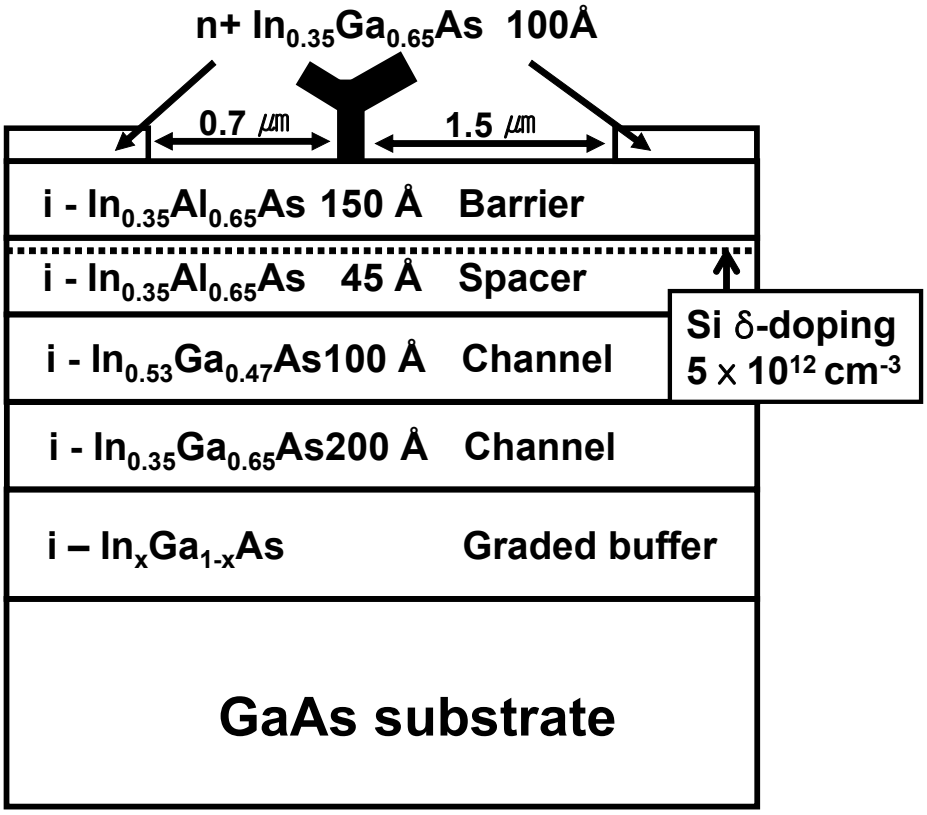

Figure 2.2 Epitaxial layer structure of the metamorphic HEMT used in this thesis.

Ⅲ. Electrical Characteristics

A. DC Characteristics

The electrical characteristics of the metamorphic HEMT used in this thesis are experimentally investigated. Fig. 3.1 shows drain currents (I_D) as function of applied drain voltages (V_D) at different gate voltages (V_G). In a fiel-effect transistor, with increasing drain voltages, drain currents initially increase and start to saturate at a certain drain voltage. However, in Fig. 3.1, the drain current of the metamorphic HEMT suddenly increases in saturation region. This anomalous increase in drain current is well known as kink phenomenon [13, 14]. The kink effect is attributed to deep level traps, impact ionization and hole accumulation. In an InAlAs/InGaAs device, deep level traps are located at the buffer or barrier layer. The carriers that injected into the deep level trap limit the drain current because they remain unavailable for conduction. When the transistor is biased in the ohmic region the trap level is nearly empty. However, as V_D is increased above the knee, the quasi-Fermi level pass through the trap level filling the traps with electrons. Once they are full, they can no longer affect the current flow and the drain current increases sharply. In addition, with increasing

drain voltages, impact ionization occurs in high electric field region of the metamorphic HEMT due to small band gap energy of the $In_{0.53}Ga_{0.47}As$ channel. The generated holes due to impact ionization are accumulated at the source region and it shifts the threshold voltage of the device, consequently additional drain currents are generated. This kink effect can induce gain reduction and excess noise at high frequencies in the device.

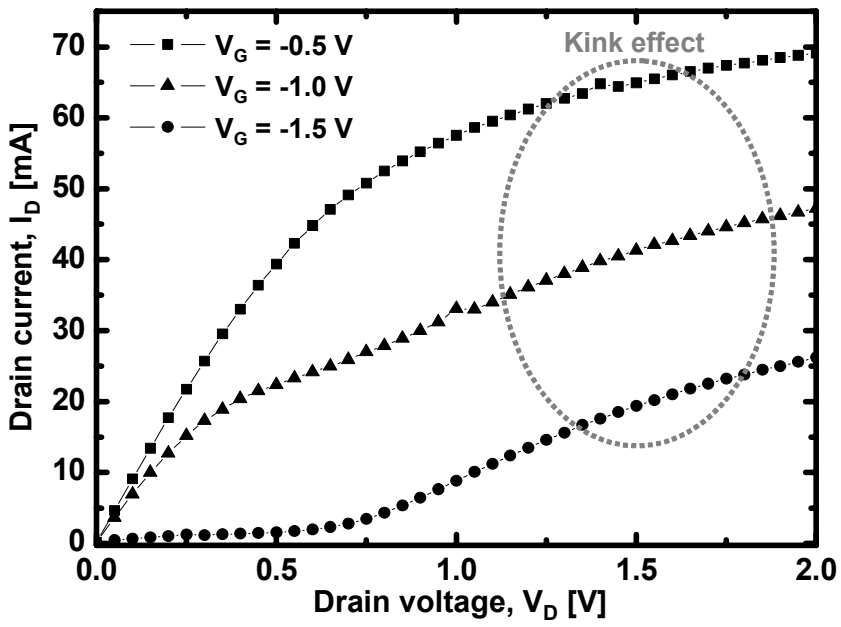

Figure 3.1 Drain currents as function of drain voltages at different gate voltages: V_G = -0.5 V, V_G = -1.0 V and V_G = -1.5 V

Fig. 3.2 shows drain currents and transconductance as function of gate voltages under different drain voltage conditions. As mentioned in previous chapter, the gate voltage controls the carrier concentration of the 2DEG. If the negative voltage is applied to the gate electrode, the width of potential well becomes wide and the electron concentration of 2DEG is decreased. As decreasing the gate bias below threshold voltage, the carrier concentration in the channel becomes negligible and the device turned off. The threshold voltage of -1.3V is measured in the metamorphic HEMT as shown in Fig. 3.2 (a).

The transconductance of the device is the most important quality factor for microwave application. The high transconductance will provide greater gain and superior high frequency performance [9]. The transconductance is defined as the slope of the I_D-V_D curve with the drain voltage held constant and is expressed as [9]

$$g_m = \left.\frac{dI_D}{dI_G}\right|_{V_D=constant} \tag{3-1}$$

The maximum transconductance of the metamorphic HEMT used in this thesis is about 520 mS/mm as shown in Fig.3.2 (b).

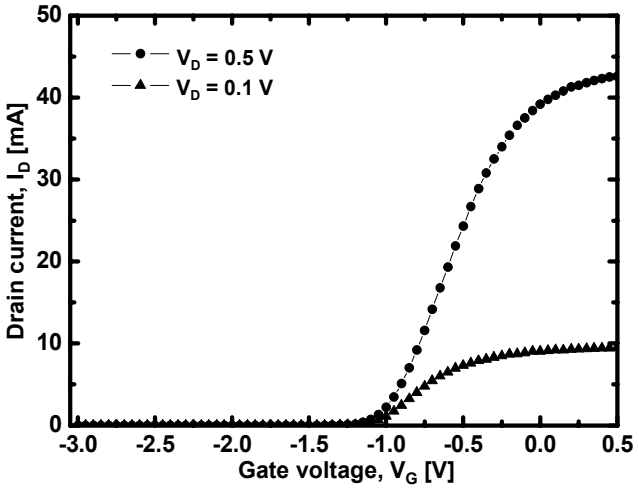

(a)

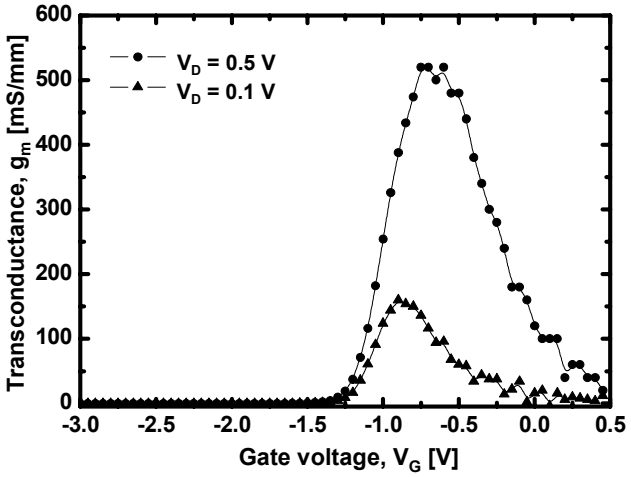

(b)

Figure 3.2 (a) Drain currents versus gate voltage at V_D = 0.1 V and V_D = 0.5 V. (b) Transconductance versus gate voltage at V_D = 0.1 V and V_D = 0.5 V.

The gate leakage currents are also measured under different bias conditions. Fig. 3.3 (a) and (b) show gate currents as function of drain and gate voltages, respectively. In the metamorphic HEMT, the gate currents are composed of electron currents due to tunneling and hole currents caused by impact ionization [15, 16]. The electron tunneling occurs at the large negative gate voltage because of the reduced gate Schottky barrier width and high electric filed. In addition, the impact ionization takes place in drain side of the gate region due to high electric field and generates electron-hole pairs. With the help of large negative gate voltage, generated holes can be swept to the gate electrode. In Fig. 3.3, it is observed that the gate leakage current is increased when the high drain and large negative gate voltage are applied to the device.

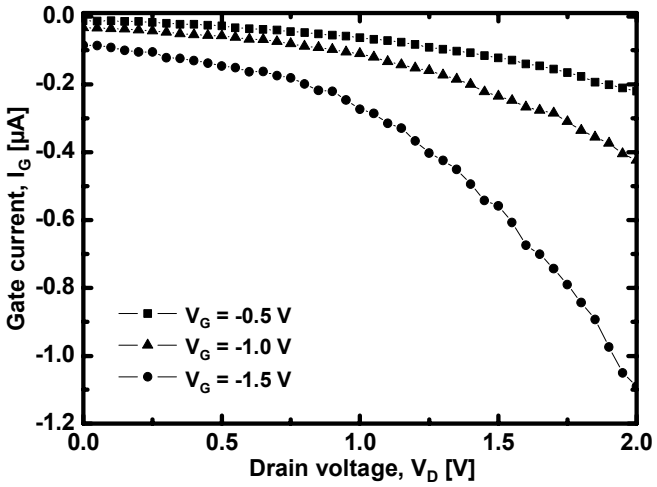

(a)

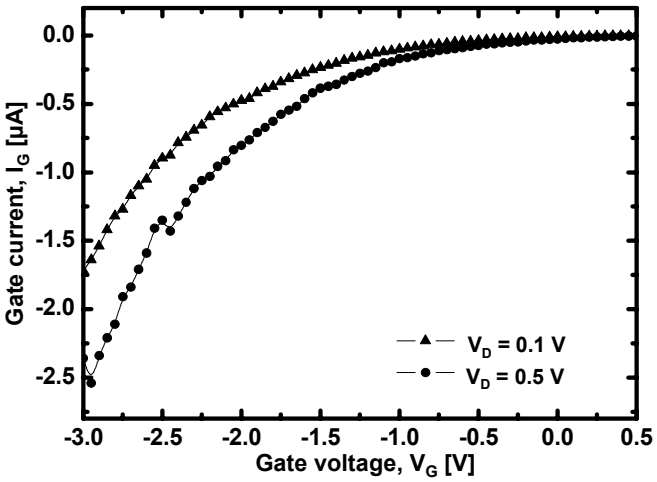

(b)

Figure 3.3 (a) Gate currents as function of drain voltages at V_G = -0.5 V, V_G = -1.0 V and V_G = -1.5 V. (b) Gate currents as function of gate voltages at V_D = 0.1 V and V_D = 0.5 V.

B. Microwave Characteristics

In this section, the microwave characteristics of the metamorphic HEMT are explained. As mentioned early, the metamorphic HEMT provides microwave gain in wide frequency ranges due to its high speed carrier transport property. For examining the microwave characteristics of the device, S-parameters of the device are measured using a vector network analyzer, HP 8563E. In a microwave transistor, the current gain cut-off frequency (f_T) and maximum oscillation frequency (f_{max}) are important factors, which determine the operating frequency. The current gain cut-off frequency (f_T) is defined as the frequency where the short-circuit gain approximates unity and the maximum oscillation frequency (f_{max}) is the frequency where the maximum available power gain of the transistor is equal to 1 [17]. In Fig. 3.4, the current gain cut-off frequency (f_T) of 60 GHz and maximum oscillation frequency (f_{max}) of 130 GHz are estimated from the measured S-parameter values at V_D = 1.5 V and V_G = -1.0 V.

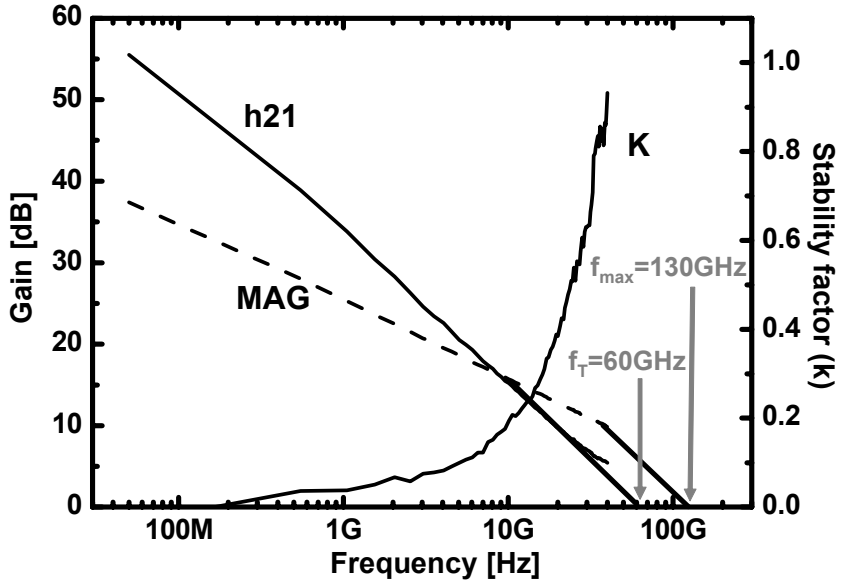

Figure 3.4 Microwave characteristics of the metamorphic HEMT: short-circuit gain (h21), Maximum available gain (MAG) and stability factor (k) at V_D = 1.5 V and V_G = -1 V.

Ⅳ. Photodetection Characteristics

A. Photodetection Mechanisms

In the metamorphic HEMT, the photovoltaic and photoconductive effects are major photodetection mechanisms [18-22]. When the optical signal is illuminated to the device, these two mechanisms influence to photodetection process simultaneously. However, according to bias condition, one of them becomes dominant.

(B.1) Photovoltaic effect

Fig. 4.1 shows the basic operation of the photovoltaic effect in the metamorphic HEMT. In the channel layer of $In_{0.53}Ga_{0.47}As$ material, optical signal is absorbed and then electron-hole pairs are generated. Under the strong electric field caused by drain voltage, photogenerated electrons and holes drift toward the drain and source region, respectively as shown in Fig 4.1 (a). Thus, photogenerated holes are accumulated in the source region. In the source region, electrons and holes are separated spatially due to internal electric field formed by energy band bending as shown in Fig. 4.1 (b). In the metamorphic

HEMT, this accumulation of photogenerated holes induces internal photovoltage and, consequently, threshold voltage shift. The threshold voltage shift due to the photovoltage is expressed as [18, 19]

$$\Delta V_{TH} = \frac{nkT}{q} \ln\left(1 + \frac{\eta q P_{opt}}{I_{pd} h\nu}\right) \tag{4-1}$$

where

$\frac{kT}{q}$ thermal voltage

η quantum efficiency in the $In_{0.53}Ga_{0.47}As$ channel

P_{opt} incident optical power

$h\nu$ photon energy

I_{pd} dark current for holes

Accordingly, this threshold voltage shift produces photocurrents in the drain terminal and it is described by

$$I_{ph,pv} = G_m \Delta V_{TH} \tag{4-2}$$

where G_m is the transconductance of the metamorphic HEMT.

In summary, the accumulation of photogenerated holes under

illumination makes the photovoltage hence it modulates the gate voltage effectively. The photodetection mechanism of the photovoltaic effect is identical to the intrinsic gain process of the metamorphic HEMT. The small gate voltage changes induce large drain currents, which are associated with transconductance as described in Eq. 4-2. Therefore, the metamorphic HEMT has internal gain provide by the photovoltaic effect as a phototransistor.

Because the photocurrent caused by the photovoltaic effect is dominated by accumulated holes, the response time is limited by the lifetime of photogenerated holes. The detected signal power can be expressed in terms of the lifetime of accumulated holes in the following manners [18].

$$P_{\det,pv} = \frac{P_{dc}}{1+\omega^2\tau_p^2} \tag{4-3}$$

where

P_{dc} photodetected signal power under dc optical signal illumination

ω angular frequency given by $2\pi f$

τ_p the lifetime of accumulated holes

In this case, the 3-dB-down frequency is given by $1/2\pi\tau_p$.

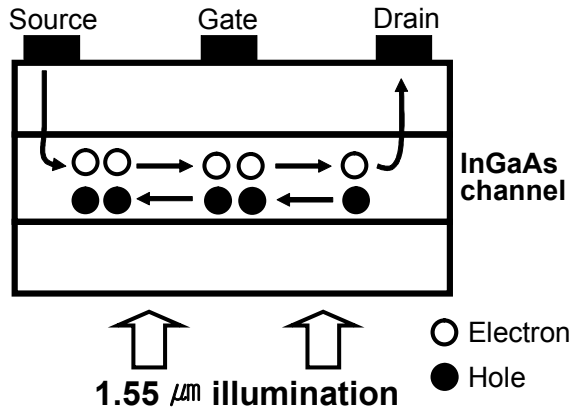

(a)

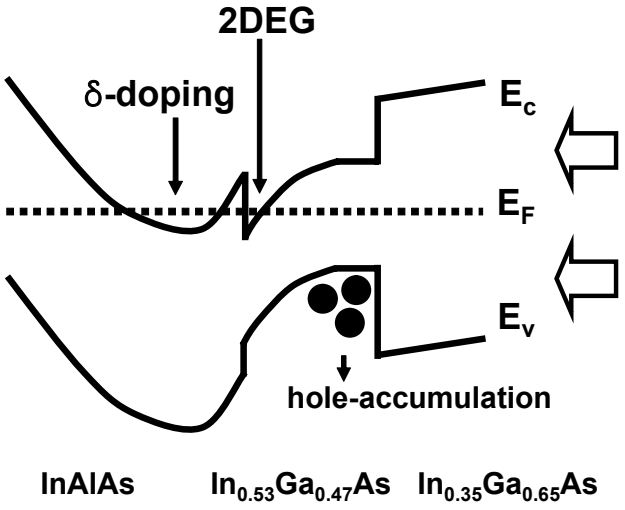

(b)

Figure 4.1 Operation of the photovoltaic effect: (a) Simple device structure, (b) Energy band diagram at the heterointerface of the source; E_c is conduction band, E_v is valance band and E_F is Fermi-level of the device.

(B.2) Photoconductive effect

In general, when the incident photon energy is greater than the band gap energy of semiconductor material, photons are absorbed in the semiconductor and electron-hole pairs are generated. Accordingly, the photogenerated carriers increase the conductivity of the material. This increased conductivity due to the optical absorption is called the photoconductive effect [23]. The photoconductive effect is dominant photodetection mechanism for photoconductors. In the metamorphic HEMT, the increased conductivity in the channel layer can generate additional drain current. The photocurrent caused by the photoconductive effect is related to increased carrier concentration in the channel and applied electric filed. It can be expressed as

$$I_{ph,pc} = (q\mu_n n\mathrm{E})WD \tag{4-4}$$

where

μ_n electron mobility in the InGaAs channel

n electron concentration generated by photodetection

E applied electric field in the channel

W, D width and depth of active region

In Eq. 4-4, the concentration of photogenerated electrons is proportional to the incident optical power thus Eq. 4-4 can be modified as

$$I_{ph,pc} \propto (q\mu_n P_{opt}\mathrm{E})WD \tag{4-5}$$

where P_{opt} is the incident optical power.

As described in Eq. 4-5, the photocurrent caused by the photoconductive effect is proportional to the incident optical power on the contrary to the photocurrent due to the photovoltaic effect, which increases logarithmically with increasing the incident optical power as expressed in Eq. 4-1.

Since the photoconductive effect is only attributed to the increased electron concentration in the channel, the photoresponse is restricted by electron lifetime. As a result, the photoconductive effect is a faster process than the photovoltaic effect.

When the photoconductive effect is involved in the photodetection process, the metamorphic HEMT can provide the photoconductive gain as in a photoconductor. Before photogenerated electrons recombine with holes, they continue to transit the channel region and the photoconductive gain is produced [23]. The photoconductive gain can

be expressed as [18, 23]

$$G_{pc} = \frac{I_{ph,pc}}{I_{prime}} = \frac{\tau_n}{t_n} = \frac{t_p}{t_n} \tag{4-6}$$

where

I_{prime} primary photocurrent, which indicates actually absorbed optical signal

τ_n electron lifetime

t_n electron transit-time in the channel

t_p hole transit-time in the channel

In the Eq. 4-6, the electron lifetime can be replaced with the hole transit-time because electrons are no longer supplied from the source until holes reach the source region. [18]. Using the Eq. 4-6, primary photocurrents that are due to absorbed optical power from the device can be estimated through the calculation of the photoconductive gain in the metamorphic HEMT.

B. Experimental Setup

The photodetection characteristics of the metamorphic HEMT are experimentally investigated. Fig. 4.2 shows the experimental configuration for the measurement of photocurrents and optical modulation response. The wavelength of 1552.5 nm distributed feedback laser diode (DFB-LD) whose 3-dB bandwidth is about 10 GHz was direct modulated and then amplified with Erbium-doped fiber amplifier (EDFA) for compensating optical coupling loss due to reflection and diffraction. The optical signal was illuminated from the substrate of the metamorphic HEMT with a lensed fiber. Since 1.55 ㎛ optical signal is transparent to the substrate, buffer layer and $In_{0.35}Ga_{0.65}As$ channel, optical absorption only takes place in $In_{0.53}Ga_{0.47}As$ channel layer. The estimated coupling efficiency is less than 10 %. Bias voltages were applied to the device using the semiconductor parameter analyzer, HP 4145B. For the accurate measurement of optical modulation response, calibration of the DFB-LD is performed first with calibrated photodiode whose 3-dB bandwidth is more than 20 GHz. The photodetected signals were measured at the drain port using the RF spectrum analyzer, HP 8563E.

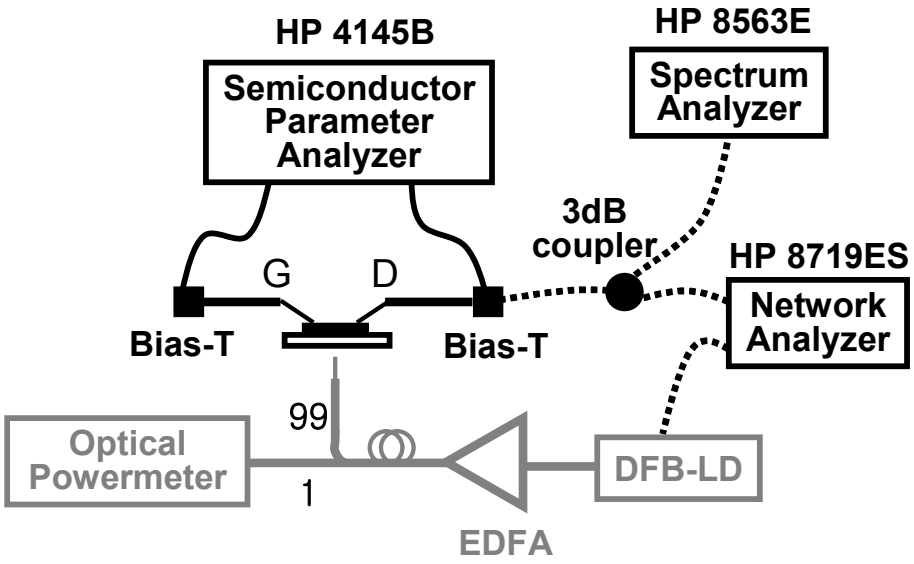

Figure 4.2 Experimental setup.

C. Photodetection under DC Optical Signal Illumination

Fig 4.3 shows I_D-V_D characteristics under dark and illuminated condition with different amounts of optical power at V_G = -0.5 V. With increasing the incident optical power, drain currents increase due to the photodetection processes including the photovoltaic and photoconductive effect. In addition, it is observed that the kink effect is suppressed under optical illumination [18, 24]. It is due to photon-induced emptying of trap level as well as changes of the hole concentration in linear region of I_D-V_D curve. In addition, because the accumulation of photogenerated holes has the same effect as the generation of holes by impact ionization, the hole accumulation under illumination causes not only threshold voltage shift but also small decrease in the source resistance.

Fig 4.4 shows I_D-V_G curve under dark and illuminated condition with different amounts of optical power at V_D = 0.5 V. As can be seen, when the gate bias is higher than the threshold voltage (turn-on condition), I_D increases and the threshold voltage of the device shifts negatively. It is well known to be due to the photovoltaic effect [18, 19]. Furthermore, it can be observed that there is small increase in the drain current under turn-off condition, the gate bias below the threshold voltage, as shown

in the inset of Fig. 4.4. This photocurrent under turn-off condition is caused by the photoconductive effect in which photogenerated electrons increase the channel conductivity and, consequently, the drain current. It is because the transconductance of the metamorphic HEMT goes to zero and the photovoltaic effect becomes negligible when the device operates in turn-off condition. The identification for photocurrents can be confirmed by fitting the measured data with the relationship between the photocurrent and incident optical power for each mechanism. Fig. 4.5 shows the photocurrents at the drain port as function of incident optical power and fitted result to Eq 4-2 and Eq. 4-5. The fitted data for turn-on condition in Fig. 4.5 clearly shows the characteristic logarithmic dependence, which indicates the dominant photovoltaic effect. On the other hand, the fitted data for turn-off condition shows clear linear dependence, confirming that the photoconductive effect is the responsible photocurrent generation mechanism.

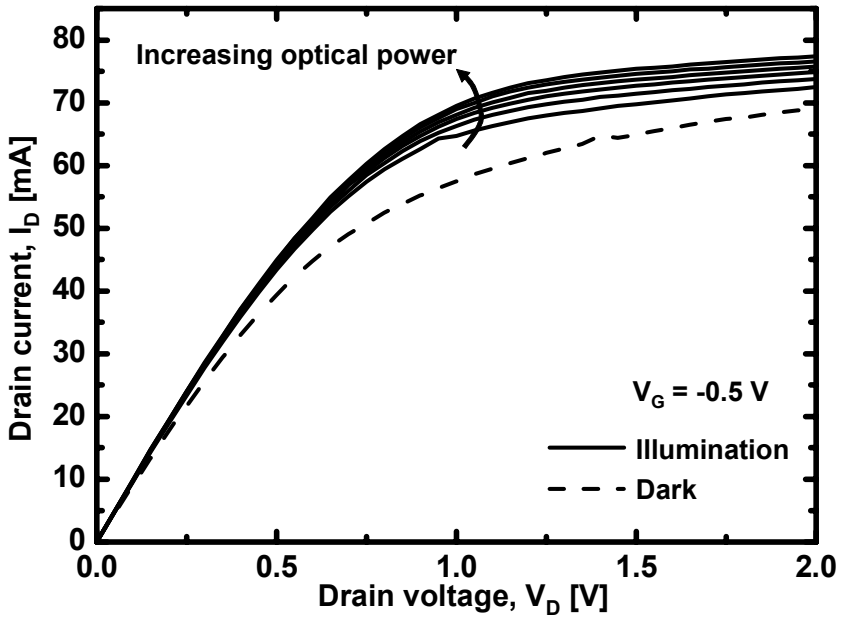

Figure 4.3 Drain currents as function of drain voltages at V_G = -0.5 V under dark and illuminated condition. The incident optical power increases from 10 mW to 60 mW with 10 mW increments, from bottom to top.

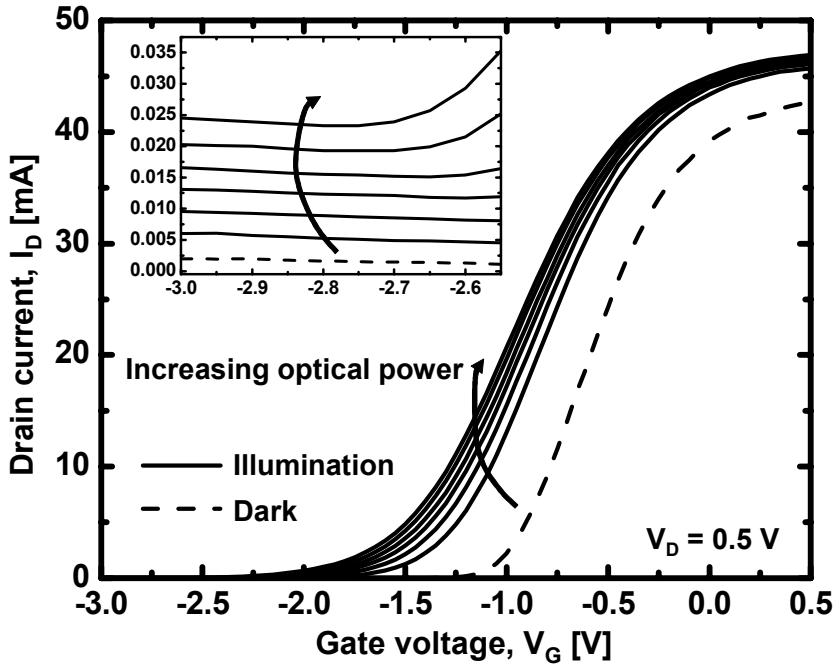

Figure 4.4 Drain currents as function of gate voltages under dark and illuminated condition at V_D = 0.5 V. The incident optical power increases from 10 mW to 60 mW with 10 mW increments, from bottom to top. The inset is enlarged graph at the gate bias below the threshold voltage, which is turn-off condition.

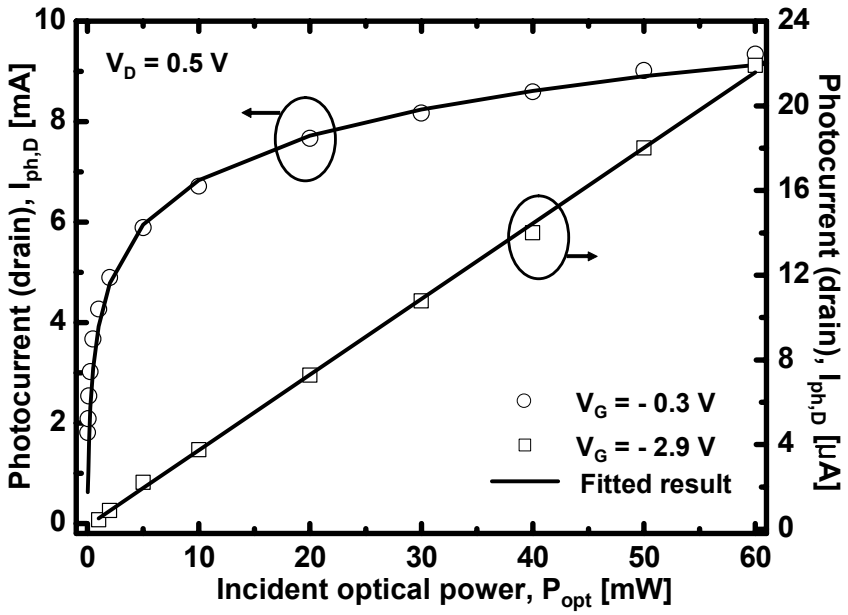

Figure 4.5 Photocurrents at drain port as function of incident optical power at V_G = -0.3 V (turn-on) and V_G = -2.9 V (turn-off) under fixed drain voltage of 0.5 V. The symbols represent measured data and solid lines indicate the fitted result to Eq. 4-2 and Eq 4-5 under turn-on and turn-off condition, respectively.

The gate leakage currents under dark and illuminated condition are also investigated. Fig 4.6 shows the gate current as function of applied gate voltages with different amounts of optical power at V_D = 0.5 V. The measured result described that gate leakage currents increase as the incident optical power and negative drain voltage increases. As mentioned in the previous chapter, the gate currents consist of electron and hole currents. However, the photocurrents at the gate port in the metamorphic HEMT are only attributed to hole currents because the optical absorption only changes the hole concentration in the channel. With the help of negative gate voltage, the photogenerated holes are swept to gate electrode. Therefore, the photocurrents at the gate port are dominated by the photoconductive effect and the device operates as a schottky photodiode. When the applied gate voltage is enhanced negatively, large amount of holes can move to the gate electrode surmounting the potential barrier of valence band and large photocurrents generated. The photodetection mechanism of the photocurrent at the gate port is also affirmed by Fig. 4.7. The linear dependence of the photocurrent on the incident optical power verifies that the photoconductive effect is dominant photodetection mechanism.

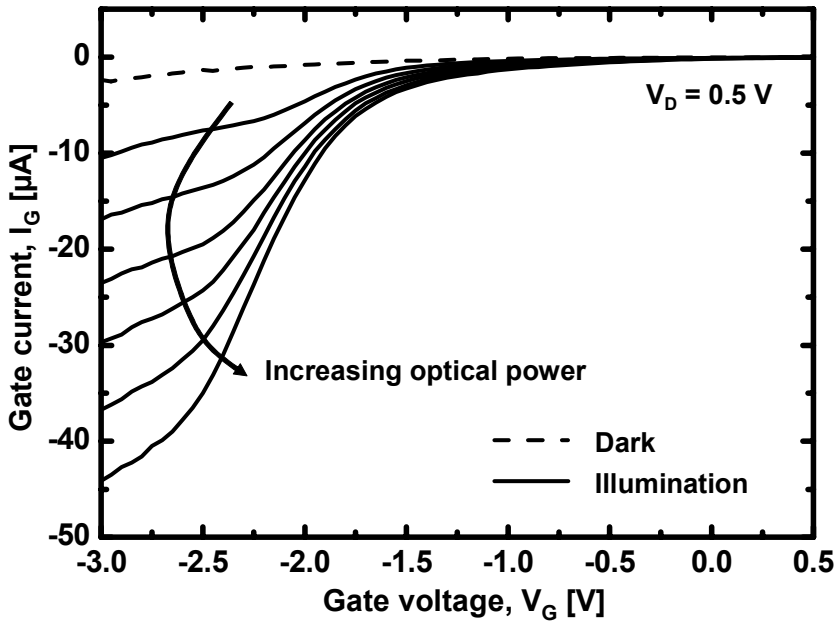

Figure 4.6 Gate current as function of gate voltages at V_D = 0.5 V under dark and illuminated condition. The incident optical power increases from 10 mW to 60 mW with 10 mW increments, from top to bottom.

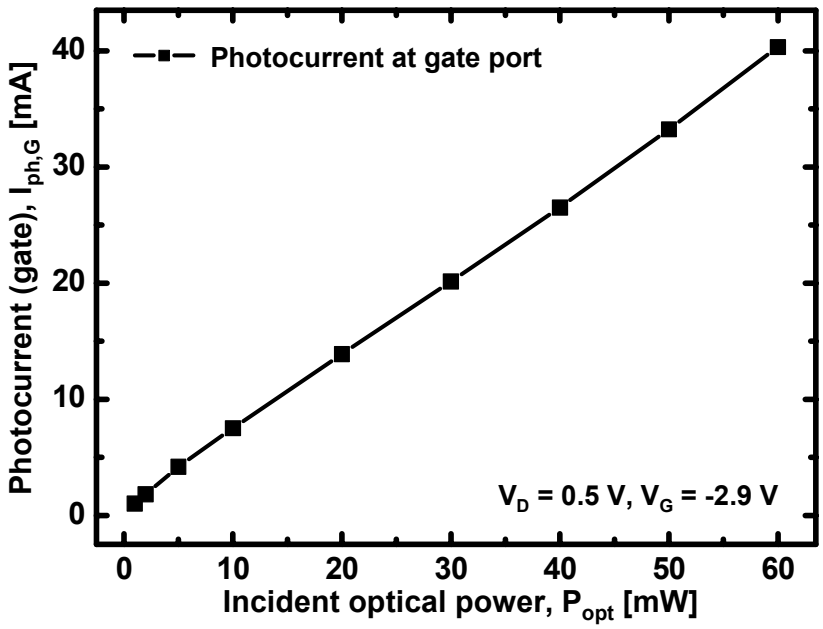

Figure 4.7 Photocurrents at drain and gate port as function of incident optical powers at V_D = 0.5 V and V_G = -2.9 V.

From these results, it is concluded that the photocurrent under turn-on condition is dominated by the photovoltaic effect. On the contrary, the photocurrent under turn-off condition is only attributed to the photoconductive effect. Furthermore, the photocurrent at the gate port is caused by the photoconductive effect.

Under turn-on condition, the photogenerated holes are accumulated in the source region and induced photovoltage takes part in the intrinsic gain mechanism of the metamorphic HEMT, which is related to transconductance. As a result, the metamorphic HEMT provides internal gain as a phototransistor (Tr-mode). In contrast, under turn-off condition, the photoconductive effect becomes dominant photodetection process because the device does not perform a transistor operation any more. In this condition, the metamorphic HEMT operates as a photoconductor (PC-mode). In addition, the photocurrent at the gate port is also attributed to the photoconductive effect and the device operates as a schottky photodiode.

D. Photodetection under Modulated Optical Signal Illumination

The photodetection characteristics under illumination of modulated optical signals are investigated. Fig. 4.8 shows the photodetected signal spectrum under illumination of 1 GHz modulated optical signal at V_D = 1.5 V and V_G = -1.0 V. The average incident optical power is 17 dBm and optical modulation index is about 0.8 when 1 GHz, 15 dBm RF signal is used to modulate the DFB-LD. The responsivity of the metamorphic HEMT as a photodetector is measured in this experiment. The responsivity indicates the performance of photodetector and it is defined as the ratio of incident optical power to generated photocurrent. Under illumination of 1 GHz modulated optical signal, the responsivity of 0.014 is obtained using the metamorphic HEMT as a photodetector. This poor optical responsivity is caused by optical coupling loss as described above.

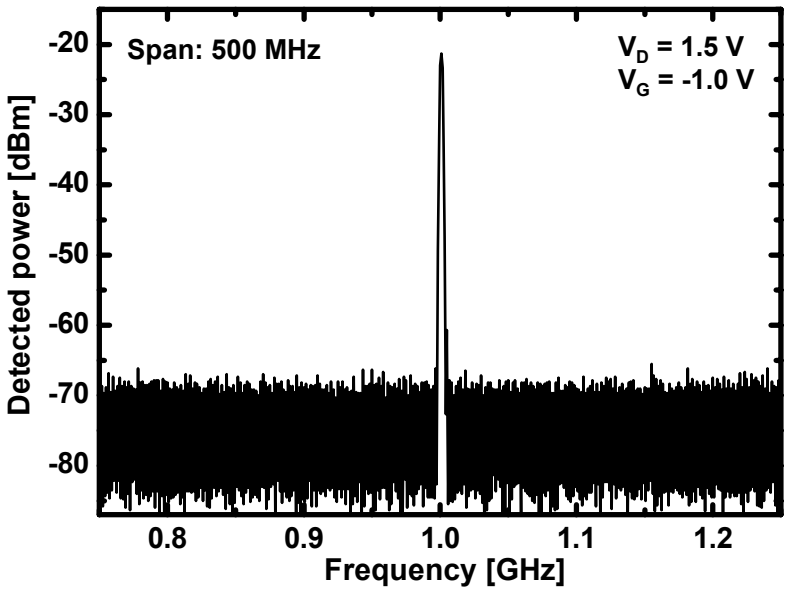

Figure 4.8 Photodetected signal spectrum of 1 GHz modulated optical signal at V_D = 1.5 V and V_G = -1.0 V.

(D.1) Optical modulation response

The optical modulation responses of the metamorphic HEMT are investigated. Fig. 4.9 shows the optical modulation responses at different gate voltages, V_G = -2.0 V and V_G = -3.5 V under fixed drain voltage of 1.5 V. At V_G = -2.0 V, large photoresponse is obtained due to the internal gain provided by the photovoltaic effect although it decays fast owing to long lifetime of photogenerated holes. By fitting the measured optical modulation response to Eq. 4-3, the hole lifetime of 150 ps is estimated and 3-dB bandwidth of 1GHz is obtained in the metamorphic HEMT as a phototransistor. In contrast, at V_G = -3.5 V, the optical modulation response is very small but nearly constant in wide frequency range due to the fast photoconductive effect, which has no phototransistor internal gain because the metamorphic HEMT operates under turn-off condition. In this condition, however, the metamorphic HEMT has photoconductive gain which is described by Eq. 4-6. Using the calculation of the photoconductive gain and measurement of photodetected power caused by the photoconductive effect, the primary photodetected power, which indicates the actually absorbed optical power, can be determined. In the experiment, the photoconductive gain of about 1.6 is estimated by taking the difference

between the electron and hole saturation velocity in the channel under identical electric filed [25, 26]. Accordingly, the primary photodetected power and phototransistor internal gain are determined as shown in Fig. 4.9. The phototransistor internal gain is defined as the ratio of photodetected power in turn-on condition to the primary photodetected power under the identical optical power illumination and V_{DS} bias. As a result, the metamorphic HEMT exhibits high phototransistor internal gain of 40 dB under turn-on condition.

The optical modulation response dependent on the applied drain voltage is also described under turn-on and turn-off condition. In Fig. 4.10, as the drain voltage increases under turn-on condition of V_G = -0.5 V, the photoresponse increases owing to the increased transconductance of the device. Since the photocurrent due to the photovoltaic effect is proportional to the transconductance as expressed in Eq. 4-2, the large drain voltage causes the increase of the photoresponse due to the enhanced intrinsic gain of the device under turn-on condition. In addition, it is observed that the measured optical modulation responses are reasonably matched to Eq. 4-5 due to the dominant photovoltaic effect, which is restricted by the lifetime of accumulated holes. However, the mismatch between the measured data and fitted result is increased when the modulation frequency increases

under high drain voltage condition. These discrepancies are mainly due to the enhanced photoconductive effect. Because the photoconductive effect is relatively fast process compare with the photovoltaic effect, the photocurrents attributed to the photoconductive effect is increased at high frequency region. Furthermore, high drain voltages also enhance the photoconductive effect due to increased electric filed in the channel as expressed in Eq. 4-5.

Under turn-off condition, the optical modulation response also increases as drain voltage increases as shown in Fig. 4.11. In this condition, photocurrents are dominated by the photoconductive effect and they are affected by carrier concentration and applied electric field as explained in Eq. 4-4. Therefore, the increased optical modulation response is attributed to enhanced electric filed.

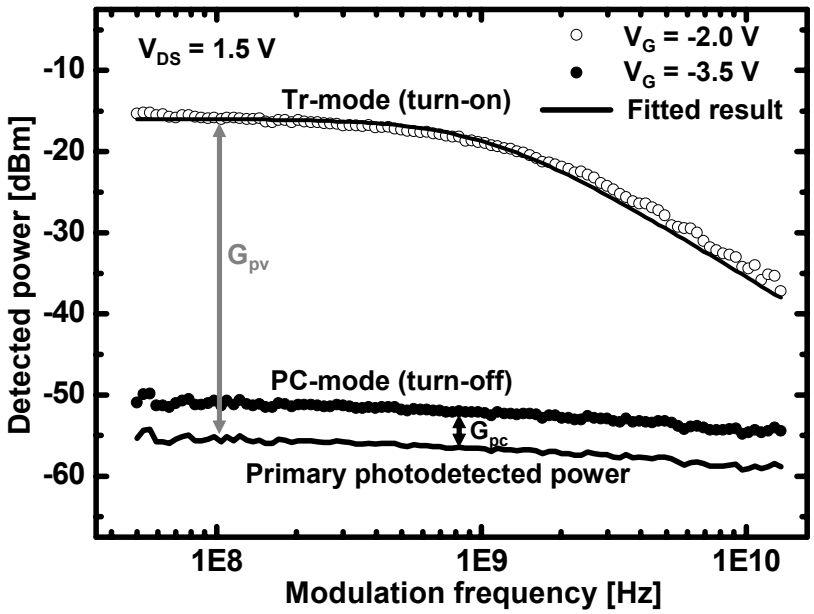

Figure 4.9 Optical modulation responses of the metamorphic HEMT at V_G = -2 V (turn-on) and V_G = -3.5 V (turn-off) under fixed drain voltage of 1.5 V. The upper solid line indicates the fitted result to Eq. 4-3 and lower one is primary photodetected power. G_{pv}: phototransistor internal gain provided by the photovoltaic effect, G_{pc}: photoconductive gain

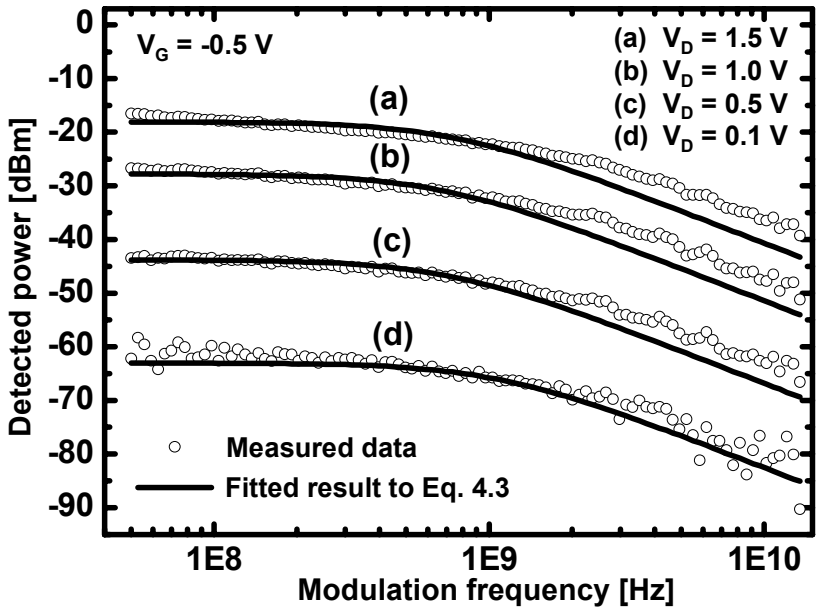

Figure 4.10 Optical modulation response of the metamorphic HEMT with different drain voltage at V_G = -0.5 V (turn-on condition). The hollow circles represent measured data and solid lines indicate fitted results to Eq. 4-3.

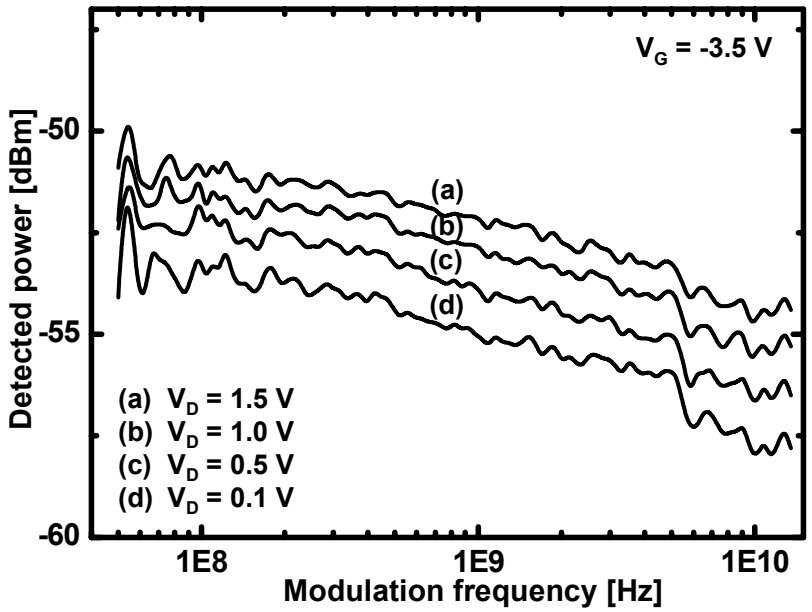

Figure 4.11 Optical modulation response of the metamorphic HEMT with different drain voltages at V_G = -3.5 V (turn-off condition).

(D.2) Bias voltage dependence

To optimize the metamorphic HEMT as a photodetector, the bias dependences of the photodetected power are examined under illumination of 10 GHz modulated optical signal. Fig. 4.12 shows the photodetected signal powers as function of drain and gate voltages. The dependences on the bias conditions are chiefly related to intrinsic gain mechanism of the metamorphic HEMT. As shown in Fig. 4.12 (a), with increasing the drain voltage, the detected power increases initially and begins to saturate. These results are similar to the transconductance characteristics of the metamorphic HEMT. Moreover, the detected power dependent on the gate voltage in Fig 4.12 (b) is also analogous to the transconductance curve although there are some discrepancies. At the large gate bias condition, turn-off condition, the detected signal power has relatively high value despite the transconductance goes to zero in this region. This increased photoresponse is due to the enhanced photoconductive effect. As explained above, the photocurrents are generated by the photoconductive effect under turn-off condition without intrinsic gain. From these results, the maximum photodetected power can be obtained at the bias voltage of maximum transconductance condition under illumination.

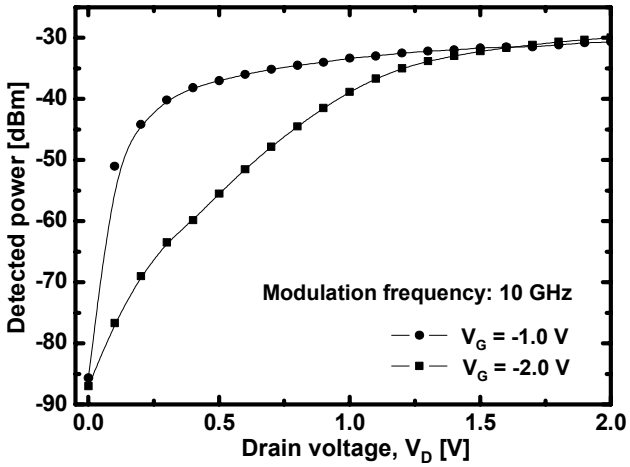

(a)

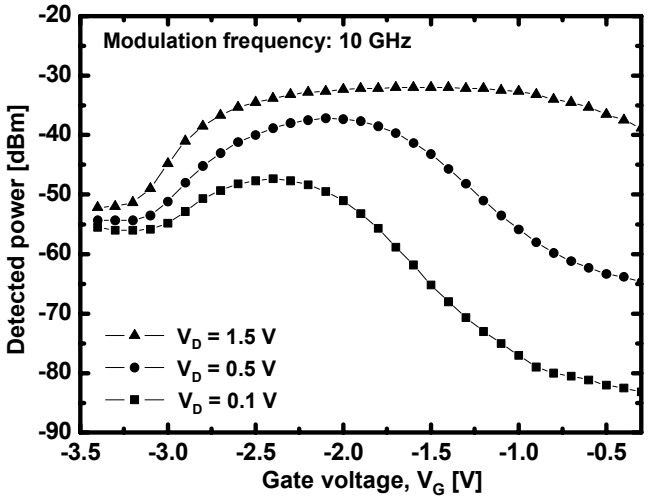

(b)

Figure 4.12 Photodetected signal powers of 10 GHz modulated optical signal as function of (a) drain voltages and (b) gate voltages.

Ⅴ. Applications for Radio-on-fiber Systems

As mentioned early, the metamorphic HEMTs can be utilized for antenna base station architecture because they can provide functionalities such as optoelectronic mixing and optical injection-locked oscillation.

A. Optoelectronic Mixer

The optoelectronic mixers based on the metamorphic HEMT have some advantages for the application of radio-on-fiber system. They can perform photodetection of 1.55 ㎛ optical signal and frequency up-conversion to millimeter-wave band simultaneously. In addition, the metamorphic HEMTs as optoelectronic mixers make it possible to realize monolithic microwave integrated circuits (MMIC) without increasing additional fabrication step. The microwave isolation of input ports is another merit of optoelectronic mixer compare with conventional microwave mixer. Using the metamorphic HEMT, the frequency up-conversion is performed and characteristics of optoelectronic mixer are examined.

(A.1) Operation principle

The metamorphic HEMT is an intrinsically nonlinear device. The main reasons for the nonlinearity in the metamorphic HEMT are nonlinear I_D-V_G characteristic and nonlinear gate-source capacitance. From these properties, the drain current of the metamorphic HEMT can be expressed as power series of the gate voltage [27, 28],

$$I_D = I_{DC} + a_1 V_G + a_2 V_G^2 + a_3 V_G^3 + \cdots \tag{5-1}$$

where

I_D drain current

I_{DC} static current

V_G applied gate voltage

a_i power series coefficients.

In the optoelectronic mixer scheme, electrical local oscillator (LO) signal is applied to the gate port for frequency up- or down-conversion and it is expressed as

$$V_{G,LO} = V_{G0} + V_S \cos(2\pi f_{LO} t) \tag{5-2}$$

where V_{G0} is bias voltage, V_S and f_{LO} is amplitude and frequency of LO, respectively.

When the optical signal is illuminated to the device, optical absorption generates the internal photovoltage due to the photovoltaic effect. The induced photovoltage can act as forward gate bias and modulate the potential barrier in the channel as explained in previous chapter. This modulated optical IF signal power and induced gate voltage ($V_{G,l}$) due to the photovoltaic effect can be described as

$$P_{opt} = P_o[1 + m\cos(2\pi f_{IF} t)] \tag{5-3}$$

$$V_{G,l} = V_{GB,l} + V_{ph}\cos(2\pi f_{IF} t) \tag{5-4}$$

where

P_o average incident optical power

m optical modulation index

f_{IF} modulation frequency

$V_{GB,l}$ dc voltage

V_{ph} amplitude of photo-voltage

Consequently, the gate voltage is composed of electrical LO signal and optical induced photovoltage,

$$V_G = V_{GB} + V_S \cos(2\pi f_{LO} t) + V_{ph} \cos(2\pi f_{IF} t) \quad (5\text{-}5)$$

where V_{GB} is total dc gate bias.

To obtain the drain current in the optoelectronic mixer, the substitution of Eq. 5-5 into Eq. 5-1 is performed. From the result of calculated drain currents, the mixing products at $f_{LO} + f_{IF}$ and $f_{LO} - f_{IF}$ are obtained as

$$I_D(f_{LO} \pm f_{IF}) \propto a_2 m P_o V_S \quad (5\text{-}6)$$

As can be seen in Eq. 5-6, the frequency up-converted signal power is proportional to optical modulation index, incident optical power, induced photovoltage and second order nonlinear coefficient.

(A.2) Implementation of frequency up-conversion

Fig. 5.1 shows the schematic diagram of frequency up-conversion using the metamorphic HEMT. The 30 GHz LO signal is applied to the gate port and the 100MHz modulated optical IF signal is illuminated to the device. The frequency up-converted signal is measured at the drain

port using the spectrum analyzer. Fig 5.2 shows the up-converted signal spectrum of the optoelectronic mixer. As shown in the output spectrum, the frequency up-conversion is successfully achieved by utilizing the metamorphic HEMT as a optoelectronic mixer.

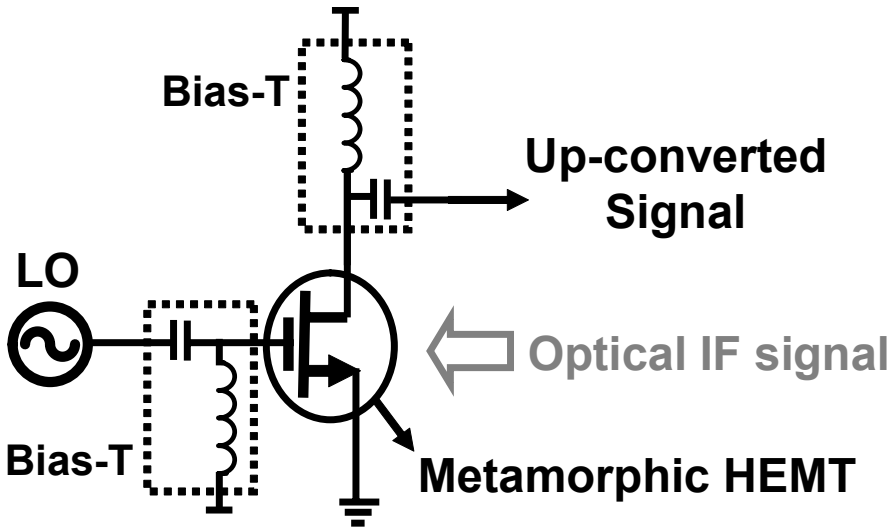

Figure 5.1 Schematic diagram of frequency up-conversion using the metamorphic HEMT.

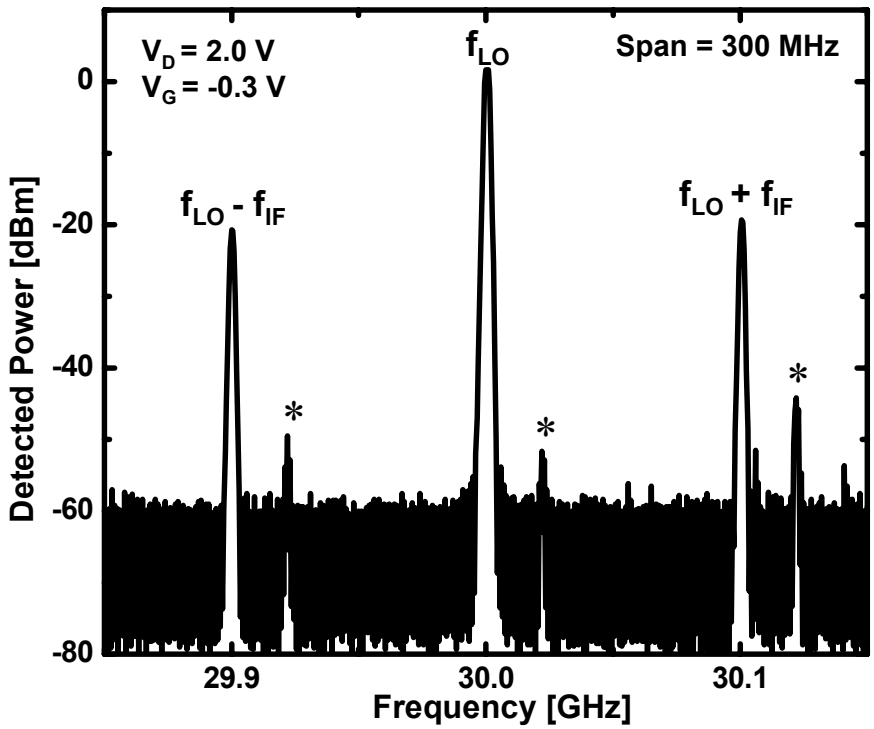

Figure 5.2 Frequency up-converted signal spectrum when LO frequency is 30 GHz and optical IF is 100 MHz. The asterisks (*) are image signals due to external harmonic mixer (HP 11970A) used for the spectrum analyzer.

(A.3) Internal conversion gain and bias dependencies

The conversion gain is one of important factors in mixers because it directly indicates the mixing efficiency. Generally, the conversion gain of microwave mixer is defined as the ratio of the output RF signal power to the input IF signal power [29]. However, in optoelectronic mixers based on metamorphic HEMTs, input signal is not determined precisely because the actually absorbed optical signal power can not measured exactly due to the ignorance of coupling loss. For this reason, the internal conversion gain is defined. The internal conversion gain of the metamorphic HEMT is defined as the ratio of frequency up-converted signal power to the primary photodetected power, which indicates the actually absorbed optical signal power without gain. This primary photodetected power can be estimated by calculating the photoconductive gain under turn-off condition as explained in previous chapter. Fig. 5.3 shows the photodetected powers and frequency up-converted signal powers as function of applied gate voltages. The primary photodetected power is obtained by subtracting the photoconductive gain from photodetected power under turn-off condition and then the internal conversion gain is determined. As mentioned above, the frequency up-converted signal ($f_{LO} + f_{IF}$) power

is related to the second order nonlinear coefficient (a_2) in Eq. 5-6 thus the mixing efficiency of the metamorphic HEMT can be affected by changing the V_G. The maximum internal conversion gain of 22.6 dB is obtained at V_D = 0.05 V. The dependence of frequency up-converted signal power on the applied drain voltages is also measured in Fig. 5.4. The frequency up-converted signal power initially increases and gets saturate at a certain drain voltage. This result is similar to the transconductance curve versus drain voltage of the metamorphic HEMT because the modulated optical signal takes part in gain process of the device due to the photovoltaic effect.

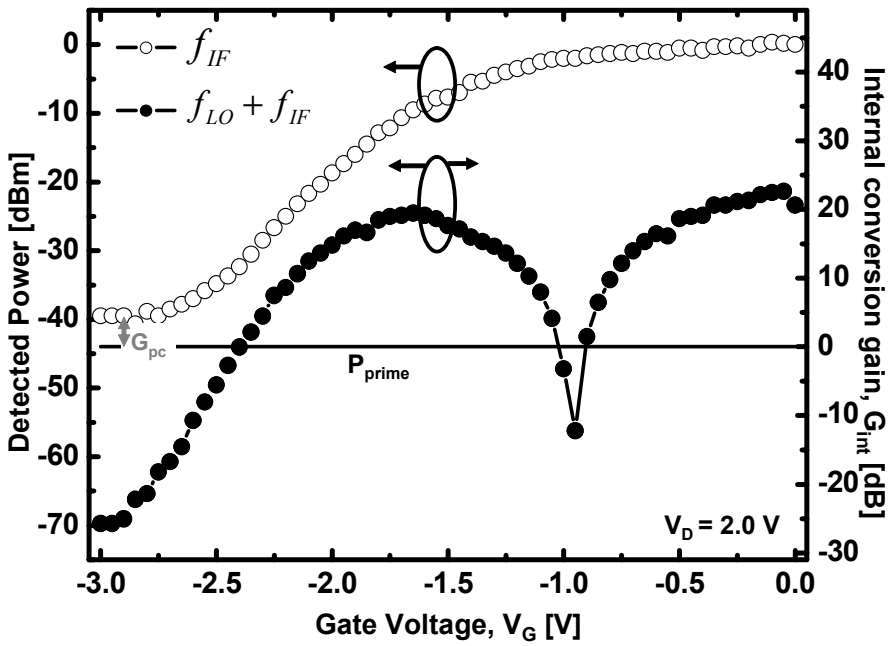

Figure 5.3 Frequency up-converted signal ($f_{LO} + f_{IF}$) power, internal conversion gain and photodetected signal (f_{IF}) power as function of gate voltages at V_D = 2 V. P_{prime}: primary photodetected power

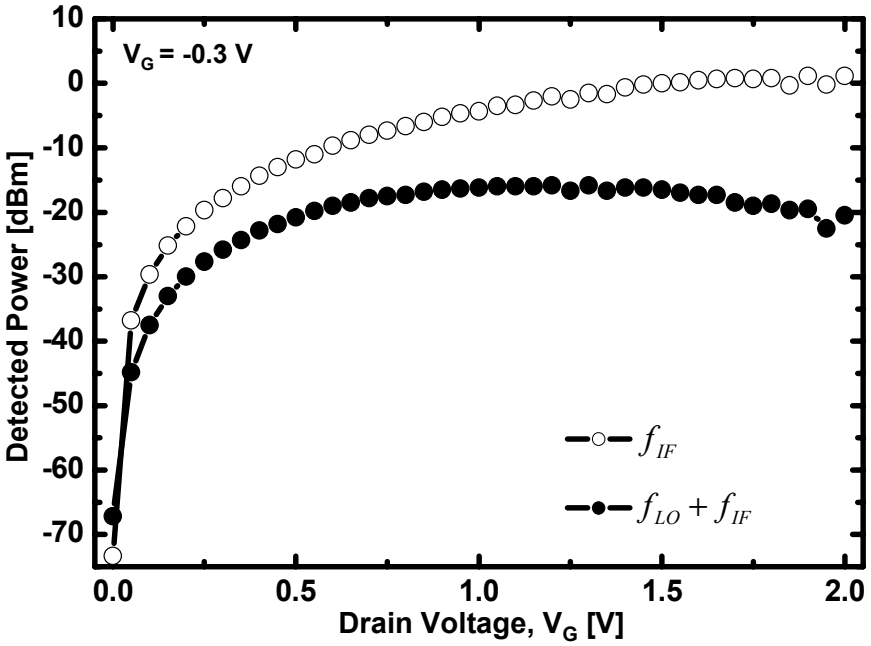

Figure 5.4 Frequency up-converted signal ($f_{LO} + f_{IF}$) and photodetected signal (f_{IF}) power as function of drain voltages at V_G = -0.3 V.

(A.4) LO frequency dependency

In order to determine the operating frequency range of the optoelectronic mixer based on the metamorphic HEMT, the mixing efficiency dependent on the LO frequency is investigated. As explained above, the LO signal is applied to the gate port and it modulate the gate voltage. Consequently, the dependences of optoelectronic mixing performance on the LO frequency are directly linked with intrinsic electrical properties of the metamorphic HEMT. Since the metamorphic HEMT exhibits excellent microwave characteristics (f_T = 60 GHz), it is expected that the optoelectronic mixing can be performed at high frequency region of LO signal. Fig. 5.5 shows the internal conversion gain as a function of LO frequency. It is seen that the internal conversion gain is nearly constant in the frequency range of 5 GHz to 40 GHz although there is small decrease due to the reduction of S21 parameter of the metamorphic HEMT and microwave components loss used in our experiments at high frequency region. From the result, it is concluded that the optoelectronic mixer based on the metamorphic HEMT can operates in wide LO frequency range, which is well extended up to millimeter-wave band with the help of high speed characteristics of the device.

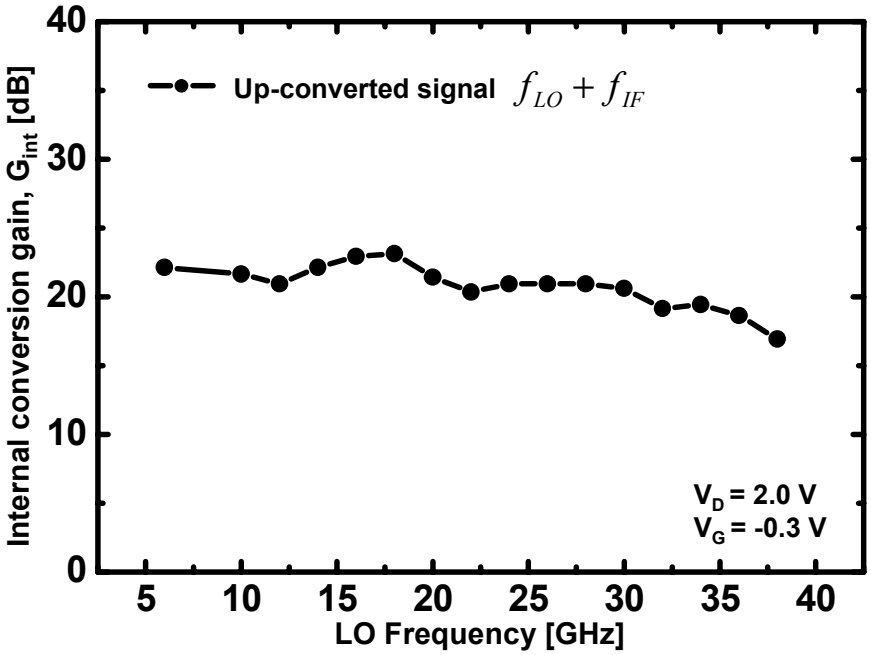

Figure 5.5 Internal conversion gain as a function of applied LO frequency at V_D = 2.0 V, V_G = -0.3 V.

(A.5) Nonlinear distortion characteristics

The nonlinear distortion characteristics of the metamorphic HEMT as an optoelectronic mixer are also investigated. In the experiment, two tone signals (f_1 = 495 MHz and f_2 = 505 MHz) were used to modulate LDs and 20 GHz LO signal was applied to the gate port of the device. Fig. 5.6 shows the frequency up-converted signal spectrum when the two-tone signal is applied. It is seen that there are two 3rd-order inter-modulation product signals (IMP3) in upper ($2f_2 - f_1$, 20.515 GHz) and lower ($2f_1 - f_2$, 20.485 GHz) side due to the inherent 3rd order nonlinearity of the metamorphic HEMT. In Fig. 5.6, the asymmetric IMP3 signals are due to asymmetry of input two tone signal power.

The SFDR is essential factor because it indicates the nonlinear distortion characteristics and determines input power range. The SFDR is defined as two-thirds the difference between the 2-tone, third-order intercept point (IP3) and the minimum discernible signal (MDS). The SFDR is expressed by following equation,

$$SFDR = \frac{2}{3} * [IP3_{OUTPUT} - MDS] \tag{5-7}$$

To obtain the SFDR of the optoelectronic mixer based on the metamorphic HEMT, the fundamental signal power and IMP3 power as a function of input RF power are measured as shown in Fig. 5.7. In this experimental condition, the noise floor is about -151 dBm/Hz and the SFDR of 96 dB· $Hz^{2/3}$ is obtained at the bias conditions of V_G = -0.3 V and V_D = 2.0 V.

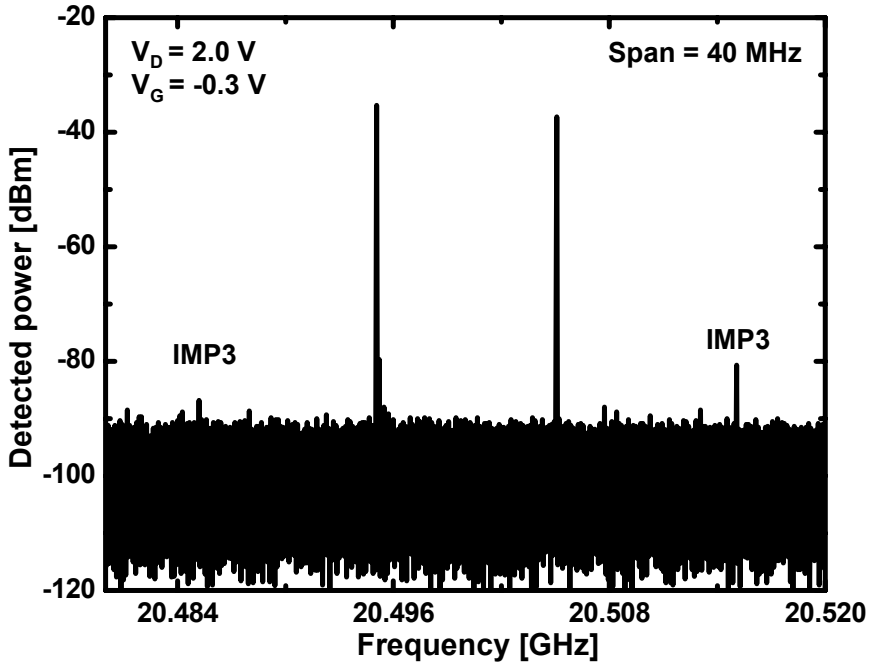

Figure 5.6 Frequency up-converted signal spectrum of two tone signal (f_1 = 495 MHz, f_2 = 505 MHz) at V_D = 2 V, V_G = -0.3 V.

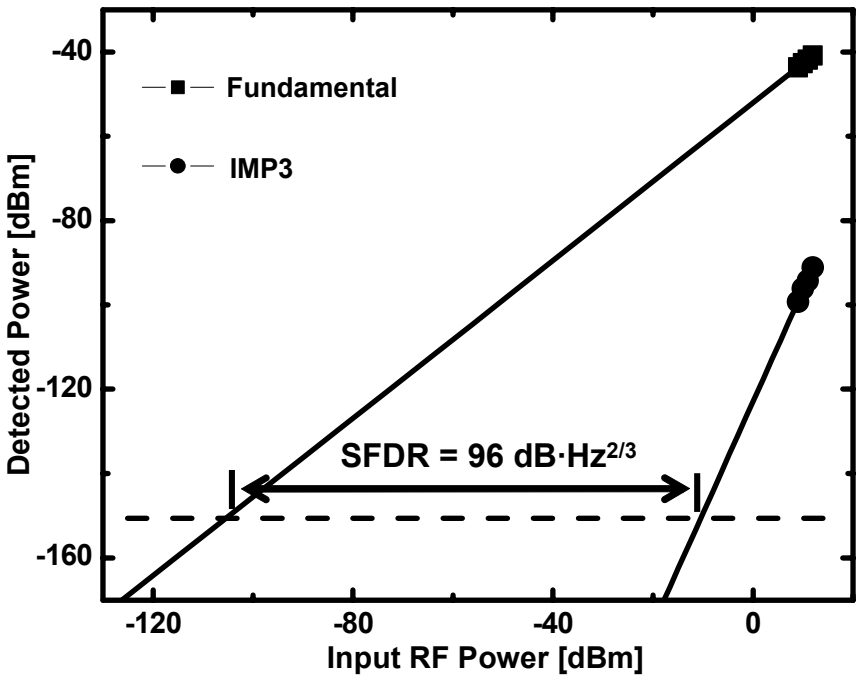

Figure 5.7 Fundamental signal and IMP3 signal power as a function of input power at $V_D = 2$ V, $V_G = -0.3$ V.

B. Direct Optical Injection-Locked Oscillator

Generally, the implementation of phase locked oscillator at high frequency region is very difficult due to the complexity of electrical circuit. To avoid this problem, the optical injection-locked oscillator is proposed [30, 31]. Using the optical injection locking technique, it is possible to realize a stable oscillator at millimeter-wave band without complex electrical circuit. In addition, the electromagnetic interference can be suppressed by using the optical signal.

(B.1) Scheme of direct optical injection-locked oscillator

In this thesis, 10 GHz direct optical injection-locked oscillator based on the metamorphic HEMT is implemented. Fig 5.8 shows schematic diagram of optical injection-locked oscillator. For frequency oscillation, feed-back loop is configured and 10 GHz band pass filter is inserted into the loop. As a result, 10 GHz free-running signal is generated. Then, modulated optical signal is illuminated to the device for optical injection locking. The optical modulation frequency of 10.24 GHz and 5.12 GHz is used for fundamental and sub harmonic locking, respectively.

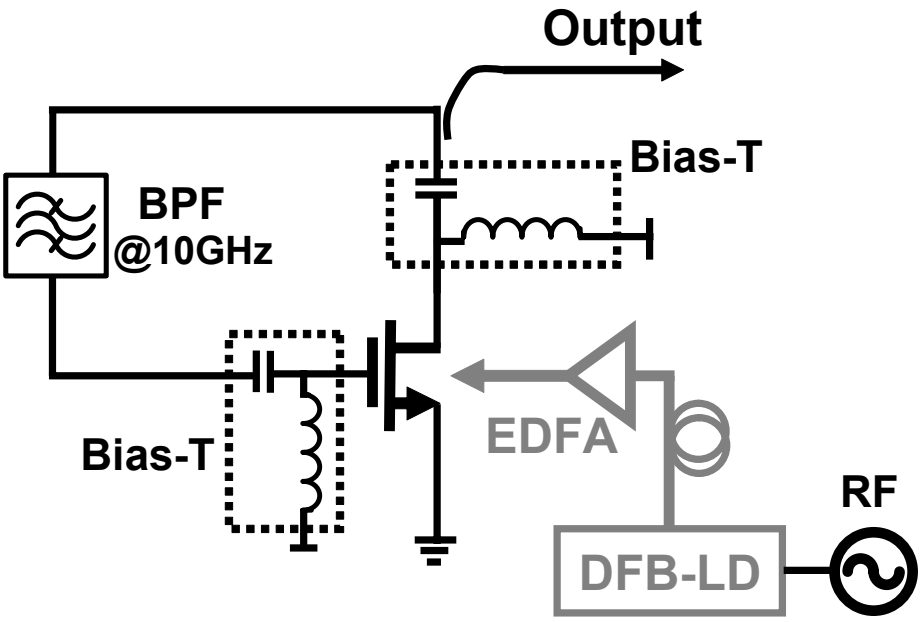

Figure 5.8 Schematic diagram of optical injection-locked oscillator. (BPF: band pass filter)

(B.2) Experimental result

Fig. 5.9 shows output spectrum of optical injection-locked oscillator. In Fig. 5.9 (a), it is seen that free-running oscillator signal is unstable and has large phase noise. When the modulated optical signal is injected to the device, the free-running oscillator is phase-locked and phase noise of output signal is suppressed as shown in Fig. 5.9 (b). Fig 5.9 (c) describes the unlocked state of optical injection-locked oscillator. Because the frequency of optically injected signal is far from the free-running oscillator frequency, there are some side bands due to mixing products of free-running and injection signal frequency.

In the injection-locked oscillator, the frequency difference between free-running oscillation signal and injection signal determines the locking process. The large frequency difference can break the locking condition of injection-locked oscillator as shown in Fig. 5.9 (c). With the purpose of investigating the injection locking characteristics, the locking range as function of incident optical powers are measured in Fig. 5.10. The locking range is defined as the frequency range of injection signal, which can lock the free-running signal. According to Adler's equation, the locking range (Δf) can be written as a function of the free-running oscillator frequency (f_{osc}) and oscillator power (P_{osc})

by [5, 32]

$$\Delta f = \frac{f_{osc}}{Q_{ext}} \left(\frac{P_{inj}}{P_{osc}} \right)^{1/2} \tag{5-8}$$

where

Q_{ext} external quality factor of the oscillator,

P_{inj} equivalent electrical power which is attributed to the photodetection process

In Eq. 5-8, the locking range depends on the power ratio of the effective injected signal power to the free-running oscillator power. Accordingly, with increasing the incident optical power, the locking range increases as shown in Fig. 5.10. In addition, the locking range of sub harmonic injection locking is very small compared to fundamental locking because of low photodetected signal power of second harmonic signal in the metamorphic HEMT as a photodetector.

As mentioned above, when the optical injection locking is successfully performed the phase noise of output signal is significantly suppressed compared with free-running oscillation signal. Fig. 5.11 shows phase noise of free-running and injection-locked state. The phase noise degradation at 10 kHz offset carrier measured from injection-

locked oscillator is about -13.5 dB. From these result, it is expected that the direct optical injection-locked oscillate based on the metamorphic HEMT can be useful for the application of radio-on-fiber system because they make it possible to generate stable oscillator signal without complex electrical circuits.

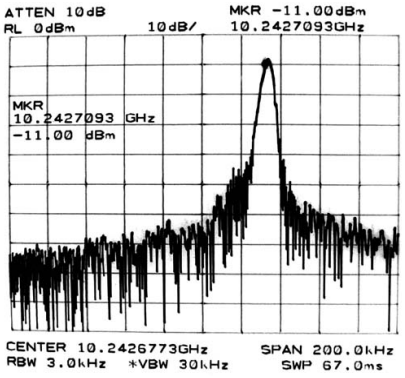

(a)

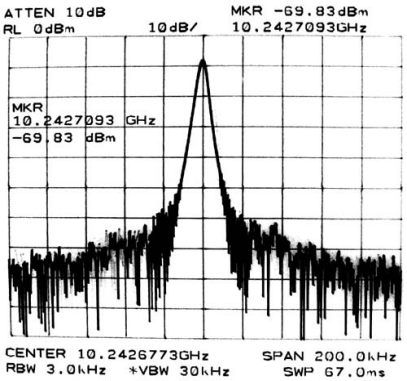

(b)

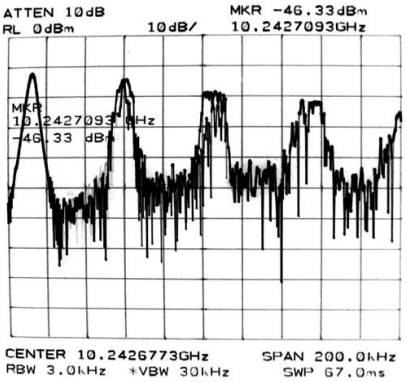

(c)

Figure 5.9 Output spectrum of optical injection-locked oscillator. (a) free-running state, (b) injection-locked state and (c) unlocked state

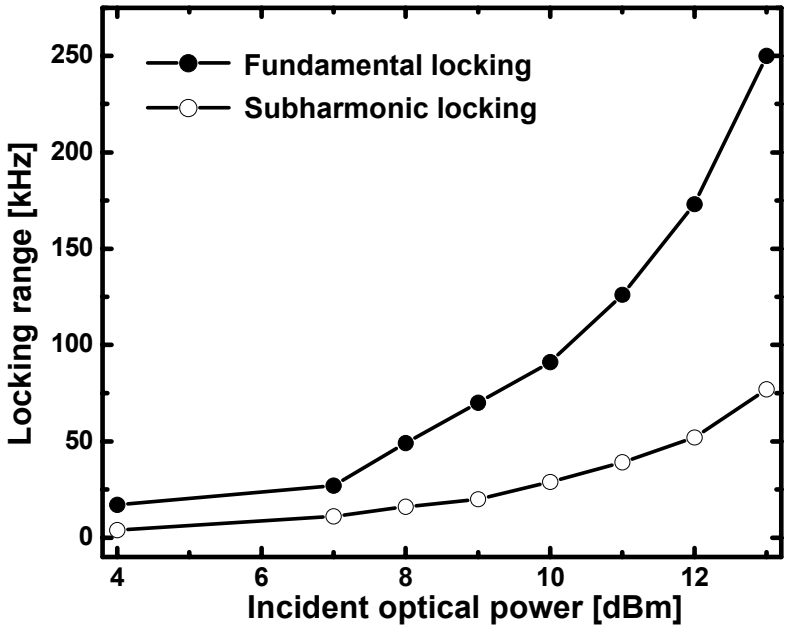

Figure 5.10 Locking range as a function of incident optical power of fundamental (solid circles) and sub harmonic signal (hollow circles).

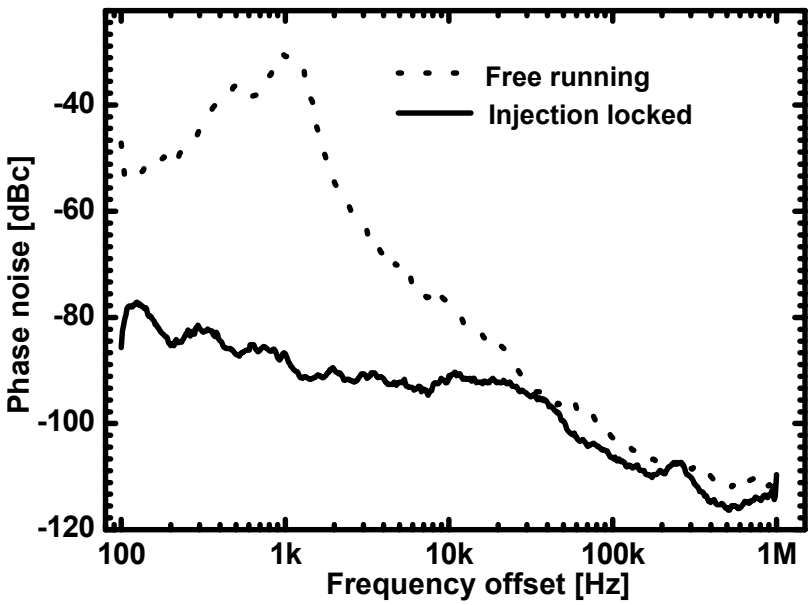

Figure 5.11 Phase noise of free-running and injection-locked oscillator.

Ⅵ. Conclusion

The photodetection characteristics of the metamorphic HEMT under 1.55 ㎛ optical illumination are investigated. There are two major photodetection mechanisms in the metamorphic HEMT which are the photovoltaic and photoconductive effect. The photovoltaic effect provides internal gain by phototransistor operation however fast-decaying optical modulation response due to long lifetime of photogenerated holes. In contrast, the photoconductive effect is fast process caused by increased channel conductivity.

It is experimentally verified that the photovoltaic effect is dominant under turn-on condition while the photoconductive effect under turn-off condition. By applying the bias voltage of turn-on and turn-on condition, photoresponses dominated by the photovoltaic and photoconductive effect are examined, respectively.

In this thesis, applications for radio-on-fiber systems are also described including optoelectronic mixer and optical injection-locked oscillator. Using the optoelectronic mixer based on the metamorphic HEMT, frequency up-conversion is implemented. It is observed that the optoelectronic mixer can operates in wide LO frequency range, which is extended up to millimeter wave band with the help of high speed

characteristics of the metamorphic HEMT. In addition, the SFDR of 96 dB· $Hz^{2/3}$ is obtained and the optimization of bias voltage is performed for the frequency up-conversion. The optical injection-locked oscillator is promising candidates for radio-on-fiber system because it can operate at high frequency region without complex electrical circuits. The 10 GHz optical injection-locked oscillator using the metamorphic HEMT is realized through fundamental and sub harmonic locking technique. The characteristics of locking range and phase noise are also observed in this scheme.

This thesis is mainly focused on the experimental investigation of photodetection characteristics of the metamorphic HEMT and its applications for radio-on-fiber system. From the results, it is expected that the metamorphic HEMT can be utilized for antenna base station architecture in radio-on-fiber system due to compatibility to the GaAs-based MMIC process. However, analytical analysis of the photodetection process and optoelectronic performance as well as experimental investigation is required for device modeling, and these remain for future works.

References

[1] A. J. Seeds, “Microwave Photonics,” *IEEE Trans. Microwave Theory and Tech.*, Vol. 50, No. 3, pp. 877-887, Mar. 2002

[2] G. Grosskopf, D. Rohde, R. Eggemann, S. Bauer, C. Bornholdt, M. Mohrle, and B. Sartorius, ”Optical Millimeter-Wave Generation and Wireless Data Transmission Using a Dual-Mode Laser,” *IEEE Photonics Tech. Lett.* Vol. 12, No. 12, pp. 1692-1694, Dec. 2000

[3] U. Gliese, S. Norskov and T. N. Nielsen, “Chromatic Dispersion in Fiber-Optic Microwave and Millimeter-Wave Links,” *IEEE Trans. Microwave Theory and Tech.* Vol. 44, No. 10, pp. 1716-1724, Oct. 1996

[4] M. J. Roberts, N. Bourhill, S. Iezekiel, D. P. Steenson and C. M. Snowden, “Optoelectronic Mixing in MMIC W-band Self-Oscillating mixer,” *Electron. Lett.*, Vol. 34, No. 9, pp. 904-905, Apr. 1998

[5] D. Yang, P. Bhattacharya, R. Lai, T. Brock and A. Paolella, ”Optical Control and Injection Locking of Monolithically Integrated $In_{0.53}Ga_{0.47}As/In_{0.52}Al_{0.48}As$ MODFET Oscillators,” *IEEE Trans. Electron Devices*, Vol. 42, No. 1, pp. 31-37, Jan. 1995

[6] K. Yuan and K. Radhakrishnan, “High Breakdown Voltage $In_{0.52}Al_{0.48}As/In_{0.53}Ga_{0.47}As$ Metamorphic HEMT Using $In_xGa_{1-x}P$ Graded Buffer”, *Proc. InP and Related Materials*, pp. 161-164, 2002

[7] F. Ali and A. Gupta, *HEMTs and HBTs: Device, Fabrication, and Circuits*, Artech House, Boston·London, 1991

[8] Wada and H. Hasegawa, *InP-Based Materials and Devices*, John Wiley & Sons, New York, 1999

[9] J. M. Golio, *Microwave MESFETs and HEMTs*, Artech House, Boston·London, 1991

[10] Y. Yamashita, A. Endoh, K. Shinohara, K. Hikosaka, T. Matsui, S. Hiyamizu and T. Mimura, “Pseudomorphic $In_{0.52}Al_{0.48}As/In_{0.7}Ga_{0.3}As$ HEMTs with an ultrahigh f_T of 562 GHz,” *IEEE Electron Device Lett.,* Vol. 23, pp.573-575, Oct. 2002

[11] S. Whelan, P. F. Marsh, W. E. Hoke, R. A. McTaggart, C. P. McCarroll and T. E. Kazior, “GaAs Metamorphic HEMT (MHEMT): An Attractive Alternative to InP HEMTs for High Performance Low Noise and Power Applications,” *Proc. InP and Related Materials*, pp. 337-340, 2000

[12] M. Chertouk, H. Heib, D. Xu, S. Kraus, W. Klein, G. Bohm, G. Trankle and G. Weimann, “Metamorphic InAlAs/InGaAs HEMTs On GaAs Substrate with Composite Chanels and f_{max} of 350 GHz,” *Proc. InP and Related Materials*, pp. 737-740, 1995

[13] T. Suemitsu, T. Enoki, N. Sano, M. Tomizawa and Y. Ishii, “An Analysis of the Kink Phenomena in InAlAs/InGaAs HEMT’s Using Two-Dimensional Device Simulation,” *IEEE Trans. Electron Devices*, Vol. 45, No. 12, pp. 2390-2399, Dec. 1998

[14] M. H. Somerville, A. Ernst and J. A. del Alamo, “A Physical Model for the Kink Effect in InAlAs/InGaAs HEMT’s,” *IEEE Trans. Electron Devices*, Vol. 47, No. 5, pp. 922-930, May. 2000

[15] R. T. Webster, S. Wu and A. F. M. Anwar, “Impact Ionization in InAlAs/InGaAs/InAlAs HEMT’s,” *IEEE Electron Device Lett.*, Vol. 21, No. 5, pp. 193-195, May. 2000

[16] G. Meneghesso, A. Di Carlo, M. Manfredi, M. Pavesi, C. Canali and E. Zanoni, “Characterization of hole transport phenomena in AlGaAs-InGaAs HEMT's biased in impact-ionization regime,” in *Conf. Device Research Digest* pp. 36-37, Jun. 1998.

[17] G. Gonzalez, *Microwave Transistor Amplifiers*, Prentice Hall, 1997

[18] Y. Takanashi, K. Takahata and Y. Muramoto, “Characteristics of InAlAs/InGaAs High-Electron-Mobility Transistors Under Illumination with Modulated Light,” *IEEE Trans. Electron Devices*, Vol. 46, No. 12, pp. 2271, 1999

[19] C.-S. Choi, H.-S. Kang, W.-Y. Choi, H.-J. Kim, W.-j. Choi, D.-H. Kim, K.-C. Jang and K.-S. Seo, “High Optical Responsivity of InAlAs/InGaAs Metamorphic High-Electron Mobility Transistor on GaAs substrate with Composite Channels,” *IEEE Photonics Tech. Lett.* Vol. 15, No. 6, pp. 846, 2003

[20] M. A. Romero, M. A. G. Martinez and P. R. Herczfeld, “An Analytical Model for the Photodetection Mechanisms in High-Electron Mobility Transistors,” *IEEE Trans. Microwave Theory Tech.* Vol. 44, No. 12, pp. 2279, 1996

[21] L. E. de Barros, A. Paolella, M. Y. Frankel, M. A. Romero, P. R. Herczfeld and A. Madjar, “Photoresponse of Microwave Transistors to High-Frequency Modulated Lightwave Carrier Signal,” *IEEE Tran. Microwave Theory Tech*. Vol. 45, No. 8, pp. 1368-1374, Aug. 1997

[22] H. Mitra, B. B. Pal, S. Singh and R. U. Khan, “Optical Effect in InAlAs/InGaAs/InP MODFET”, *IEEE Trans. Electron Devices*, Vol. 45, No. 1, pp. 68, 1998

[23] S. M. Sze, *Physics of Semiconductor Devices*, John Wiley & Sons, 1981

[24] N. Bourhill, S. Iezekiel and D. P. Steenson, "The Impact of Optical Illumination on The Breakdown Characteristics of pHEMTs," *Int. Topical Meeting Microwave Photonics, proc.*, pp. 259-262, 2003

[25] J. Dickmann, C. H. Heedt, and H. Daembkes, "Determination of the Electron Saturation Velocity in Pseudomorphic $Al_xGa_{1-x}As/In_yGa_{1-y}As$ MODFET's at 300 and 100K," *IEEE Trans. Electron Devices*, Vol. 36, No. 10, pp. 2315-2319, Oct. 1989

[26] K. Brennan, "Theory of the steady-state hole drift velocity in InGaAs," *Applied Physics Lett*. Vol. 51, pp. 995-997, Sep. 1987

[27] Paolella, S. Malone, T. Berceli and P. R. Herczfeld, "MMIC Compatible Lightwave-Microwave Mixing Technique," *IEEE Trans. Microwave Theory Tech*. Vol. 43, No. 3, pp. 518-522, Mar. 1995

[28] T. Berceli, M. Izutsu and T. Sueta, "A New Lightwave-Microwave Signal Conversion Method," *Microwave Sym. Tech. Digest* pp. 1407-1410, 1993

[29] S. A. Maas, *Microwave Mixers*, Artech House, Boston, 1993

[30] P. Callaghan, N. J. Gomes, S. K. Suresh Babu and A. K. Jastrzebski, “Optical injection locking of a microwave monolithic self-oscillating mixer,” *Electron. Lett.*, Vol. 13, pp. 1162-1163, Jun. 1997

[31] M. Karakucuk, W. Li, D. Yang, P. Freeman, J. East, G. I. Haddad and P. Bhattacharya, “Direct Optical Injection Locking of InP-based MODFET and GaAs-based HBT Oscillators,” *Conf. High Speed Semiconductor Device and Circuits Proc.* pp. 365-374, 1993

[32] R. Adler, “A Study of Locking Phenomena in Oscillators,” *IEEE Proc.*, vol. 61, no. 10, pp. 1380-1385, 1973

국문요약

Metamorphic HEMT의 광 검출 특성 및 Radio-on-fiber system에서의 응용

본 논문에서는 Metamorphic HEMT의 1.55 ㎛ 광 신호에 대한 광 검출 특성을 조사하고, radio-on-fiber system에서의 응용을 소개하였다. 우선 metamorphic HEMT의 layer 구조와 전기기적인 동작 특성을 조사하여 소자의 기본적인 특성 및 동작 조건을 파악하였다.

Metamorphic HEMT의 광 검출 특성을 밝히기 위해 photovoltaic 효과와 photoconductive 효과에 의한 광 검출 과정을 조사하였다. DC 상태와 변조된 광 신호를 주입함으로써, 각 동작 조건에서의 광 검출 작용을 명확히 규명하였다. 이를 통해 Photovoltaic 효과는 metamorphic HEMT가 turn-on 상태에서 동작하고 있을 때, photoconductive 효과는 turn-off 영역에서 주요하게 작용하는 것을 실험적으로 입증했다. 또한 bias 전압에 따른 광 검출 과정을 살펴 보았고, 광 변조 주파수 응답을

측정하였다.

Metamorphic HEMT의 radio-on-fiber system에서의 응용적인 측면으로 optoelectronic mixer와 direct optical injection-locked oscillator를 구현하였다. Metamorphic HEMT기반의 optoelectronic mixer를 이용하여, 넓은 LO 주파수 영역에서 주파수 상향 변환 수행하였고, 그것의 internal conversion gain 특성 및 비선형 왜곡 현상을 조사하였다. Direct optical injection-locked oscillator 실험을 통하여 10 GHz free-running oscillator를 metamorphic HEMT를 이용하여 구성하고, 변조된 광 신호를 주입하여 10 GHz 대역의 안정된 oscillator를 구현하였다. 또한 optical injection-locked oscillator의 locking range와 phase noise 특성을 조사하였다.

위와 같은 연구 결과를 통해 metamorphic HEMT가 radio-on-fiber system의 antenna base station에서 광 검출기 또는 광-전 응용 소자로 활용될 수 있을 것으로 기대되며 이를 통하여 antenna base station의 단일 칩 집적이 가능할 것으로 생각된다.